Cryo-ET analysis of budding yeast synaptonemal complexes *in situ*

Olivia X. Ma, Shujun Cai, Jian Shi and Lu Gan*

Department of Biological Sciences and Centre for BioImaging Sciences, National University of Singapore, Singapore 117543

* Correspondence: lu@anaphase.org

Abbreviations used:

SC: synaptonemal complex

LE: Lateral element

CR: Central region

TF: Transverse Filament

SM: Sporulation medium

cryo-ET: electron cryotomography / cryo-electron tomography

ABSTRACT

The synaptonemal complex (SC) is the large, conserved, proteinaceous scaffold that assembles between and holds together homologous chromosomes in meiotic prophase. Knowledge of the native structure of this complex is needed to evaluate how the SC carries out its functions. Traditional electron microscopy and super-resolution light microscopy have revealed that in many organisms, the SC has a ladder-like structure: two rail-like lateral elements are bridged by a set of rung-like transverse filaments. The transverse filaments are connected along their centers by a central element. To determine the 3-D architecture of the SC *in situ*, we studied frozen-hydrated meiotic yeast cell cryosections by Volta phase-contrast electron cryotomography and subtomogram analysis. We find the SC is built from triple-helical filaments that pack into dense polycrystalline bundles. These structures are also abundant in the polycomplexes of pachytene-arrested cells. Dissolution by 1,6-hexanediol treatment suggests that these triple-helical filaments belong to the central region of the SCs. Subtomogram averaging revealed that the SC's triple-helical filaments are up to 12-nm thick and have a 5-nm rise and 130-nm pitch. Single triple-helices and polymers thinner than the triple helix, such as single or double strands, were not detected, consistent with the strong self-oligomerization properties of SC proteins. The dense packing of SC subunits supports the notion that the SC's mechanical properties help coordinate the rapid end-to-end communication across synapsed chromosomes.

INTRODUCTION

Meiosis is a conserved form of cell division that underlies sexual reproduction. Diploid cells go through one round of DNA replication followed by two sequential rounds of cell division, producing gametes with half as many parental chromosomes. The first division (meiosis I) involves the segregation of homologous chromosomes while the second division (meiosis II) involves the segregation of sister chromatids. In the budding yeast Saccharomyces cerevisiae (herein called yeast), meiosis I has a prolonged prophase that is characterized by homolog pairing, formation of programmed double-stranded breaks, recombination, and maturation of crossovers. These events largely coincide with the assembly of synaptonemal complex (SC) and changes in chromosome morphology. In humans, failure of these events can cause chromosome-segregation errors and lead to severe birth defects or infertility (Zickler and Kleckner, 1999).

The synaptonemal complex is a large proteinaceous structure that holds paired homologous chromosomes close together along their lengths during meiotic prophase (Page and Hawley, 2004; Zickler and Kleckner, 2015). Furthermore, the SC is critical for the proper segregation of homologs in the absence of crossovers (Gladstone *et al.*, 2009). Traditional electron microscopy has revealed that the SC has a 100-nm-wide ladder-like organization, comprised of two parallel lateral elements (LE; the rails), which are bridged by the central region (CR) (Schmekel and Daneholt, 1995; Zickler and Kleckner, 1999) (Fig. 1A). The CR has at least two subcomponents -- the transverse filaments (TFs; the rungs), which are perpendicular to the LEs, and the central elements, which line up parallel to the LEs along the SC's

length (Zickler and Olson, 1975; Voelkel-Meiman *et al.*, 2013). Each homologous chromosome is anchored to one LE by a set of chromatin loops. Despite the weak sequence conservation of its component proteins, the SC's structural and functional features are common to most eukaryotes (Fawcett, 1956; Moses, 1956; Byers and Goetsch, 1975; Carpenter, 1975).

Many SC structural components have been characterized in yeast. These include the LE proteins Rec8, Red1, and Hop1 (Smith and Roeder, 1997; Klein *et al.*, 1999); the TF protein Zip1 (Sym *et al.*, 1993); and the central element proteins Ecm11 and Gmc2 (Voelkel-Meiman *et al.*, 2013). The LE proteins are assembled onto the chromosomes before homolog pairing occurs. The TF protein Zip1 first localizes to the centromeres during early prophase (Macqueen and Roeder, 2009), where it mediates local coupling of homologous centromeres and then the pairing and alignment of homologous chromosomes along their lengths (Zickler and Kleckner, 2015). When homologous chromosomes become closely apposed during synapsis, the SC becomes visible by EM (Zickler and Kleckner, 1999). Substantial progress has been made on the structural analysis of SC components by X-ray crystallography (Kim *et al.*, 2014; Lu *et al.*, 2014; Syrjanen *et al.*, 2014; Seo *et al.*, 2016; Dunce *et al.*, 2018; West *et al.*, 2019), electron tomography of plastic-sectioned mouse testis (Spindler *et al.*, 2019), and electron cryotomography (Cryo-ET) of recombinant human LE component SYCP3 (Bollschweiler *et al.*, 2018). These studies have shown that purified SC subunits can form large oligomers, mediated in large part by their coiled-coil regions.

While meiotic nuclei have been studied for decades by traditional EM, the 3-D macromolecular organization of the SC and chromatin is unknown *in situ* because traditional EM is susceptible to fixation, dehydration, and staining artifacts. Cryo-ET can reveal 3-D nanoscale structural information on cellular structures in a life-like frozen-hydrated state (Gan and Jensen, 2012). We used cryo-ET to visualize the organization of the yeast SC in meiotic nuclei throughout prophase. Our data shows that SCs contain densely packed bundles of protein triple-helical filaments. In late prophase (pachytene) of both wild-type and mutant cells, these bundles of triple-helical filaments are larger but do not form a stacked-ladder motif. The dense, partially ordered packing is consistent with the hypothesis that the SC has liquid-crystalline properties (Rog *et al.*, 2017) and informs models for the rapid end-to-end coordination of biochemical events along the synapsed homologous chromosomes (Zhang *et al.*, 2014).

RESULTS

The SC is a transient structure, making its analysis by low-throughput techniques like cryo-ET challenging. We therefore used diploid strains of the SK-1 background (Kane and Roth, 1974), which synchronously assemble SCs 4 to 7 hours after changing from pre-sporulation medium to sporulation medium (SM). Strains NKY611 and DK428 served as wild type (WT) while strain EW104 (*ndt80*Δ) served as a control because it arrests in pachytene (Padmore *et al.*, 1991; Xu *et al.*, 1995; Chu and Herskowitz, 1998; White *et al.*, 2004; Scherthan *et al.*, 2007). Strains DK428 and EW104 bear GFP-tagged Zip1 (White *et al.*, 2004; Scherthan *et al.*, 2007). With few exceptions, we use the terms wild-type and *ndt80*Δ instead of the strain names. To verify the synchronization, we incubated WT cells in SM and then imaged samples by fluorescence microscopy every hour. We classified the fluorescence signals based on published criteria (White *et al.*, 2004) (Fig. 1A). Diffuse Zip1-GFP fluorescence appeared in 85% of cells (n = 75) after 3 hours in SM (Fig. 1B). The fluorescence signals appear punctate at 4 hours in SM, string-like in 5 - 6 hours, start to weaken in ~ 7 hours, and were rarely visible by 8 hours (Fig. 1B). Meiosis finished after 12 hours of SM incubation, at which point 97% of the cells (n = 155) had an ascus with 4 spores. For WT cells, cultures incubated 5 - 6 hours in SM had the highest proportion mature SC-containing cells (Fig. 1C). *ndt80*Δ cells accumulate nuclear Zip1-GFP approximately 3 hours after SM incubation and then arrested in pachytene as expected (Fig. 1D).

Visualization of SCs *in situ* by cryo-ET

We performed a number of control experiments that suggest the SC has densely packed bundles of triple-helical protein filaments. First, the SC cryo-ET densities coincided with the appearance and disappearance of Zip1-GFP fluorescence through meiosis. Second, many of these structures have the dimensions expected of SCs. Third, these structures are absent in SM-treated haploid cells. Fourth, the abundance of these structures greatly increases in pachytene-arrested cells. Fifth, perturbation with a chemical known to disassemble SCs result in the depletion of these structures in the nucleus. We now present these experiments in detail.

We incubated WT cells in SM and then prepared self-pressurized-frozen samples every 2 hours for 8 hours. We then cut cryosections of these samples with nominal thicknesses of 70 or 100 nm. To increase the contrast, we collected cryo-ET data with a Volta phase plate (Fukuda *et al.*, 2015). Cryotomograms of cell nuclei at 0 hours did not contain any ~100-nm-or-larger structures expected of SCs (Fig. 2A). These cell nuclei contained 10-nm-diameter nucleosome-like particles and ≥ 20-nm-wide multi-megadalton-sized complexes (megacomplexes, such as pre-ribosomes) like those seen in cryo-ET studies of yeast, insect, and HeLa nuclei (Chen *et al.*, 2016; Cai *et al.*, 2018a; Cai *et al.*, 2018b; Eltsov *et al.*, 2018; Ng *et al.*, 2019). After 2 hours in SM, a few cells had small bundles of filaments that present a trefoil motif when view along their long axis (Fig. 2B). At 4 and 6 hours in SM, the cell nuclei contained larger bundles of filaments (Fig. 2, C and D). At least one of the dimensions of each filament bundle is 100-nm. These filament bundles were rare in cells incubated for 8 hours in SM (Fig. S1A).

We did not see any filament bundles of the kind just presented in more than 1,000 cryo-ET datasets of interphase and mitotic haploid *S. cerevisiae* cells that were incubated in rich media (Chen *et al.*, 2016; Gan *et al.*, 2019; Ng *et al.*, 2019). Recent studies showed that when stressed by glucose deprivation, components of the yeast translation machinery can form large cytoplasmic filaments (Marini *et al.*, 2018; Nueske *et al.*, 2018). SM contains the less-preferred acetate as the carbon source, which may induce stress-related structures that we have not seen before. To test if these meiotic nuclear filament bundles were stress induced, we incubated haploid cells in SM for 6 hours and then performed cryo-ET of cryosections. Haploid cells treated this way did not contain any filament bundles (Fig. S1B), further supporting the notion that these structures are part of the SC.

*ndt80*Δ cells have more SC structures than wild type cells

When incubated in SM, *ndt80*Δ cells arrest at pachytene with SCs, but continue to express SC proteins such that nearly every *ndt80*Δ cell has polycomplexes -- large aggregates of SC proteins that sometimes resemble side-by-side stacked SCs (Zickler and Olson, 1975; Sym and Roeder, 1995; Schmekel, 2000; Bhuiyan *et al.*, 2003). Because polycomplexes are rare in wild-type cells of the SK-1 genetic background (Padmore *et al.*, 1991), the *ndt80*Δ polycomplex phenotype represents a means to further test the hypothesis that the densely packed filamentous proteins are SC proteins. After 8 hours of SM incubation, *ndt80*Δ cells contained both bright fluorescent spots (polycomplexes) and string-like signals (SCs) in nearly every cell (Fig. 3A). To verify that these cells contain polycomplexes, we prepared and then imaged plastic sections of negatively stained pachytene-arrested cells. In these cells, we found stain distributions expected of the polycomplex (Zickler and Olson, 1975)

(Fig. 3B). Cryotomograms revealed that pachytene-arrested *ndt80*Δ cells have more and larger filament bundles (Fig. 3C). These SC structures do not appear like stacked ladders (Fig. S2), but their dimensions (larger than 500 nm in some cases) are consistent with polycomplexes (Dong and Roeder, 2000; White *et al.*, 2004). These extra-large filament bundles could arise from interactions between neighboring SC or from post-synapsis loaded SC proteins (Voelkel-Meiman *et al.*, 2012). The highly correlated light and electron-microscopy phenotypes in pachytene-arrested cells also supports the assignment of the meiotic nuclear filament bundles as SC structures.

Yeast meiotic nuclei have unexpected architectural features

We expected to observe cryo-ET densities that resemble a large number of ladder-like motifs, i.e., parallel rows of 100-nm-wide filaments bridging two dense rails. However, we did not find any ladder-like structures in either pachytene-arrested cells or in WT cells at any of the time points we sampled. We also did not find any of the side-by-side “stacked” ladder motifs in polycomplexes of pachytene-arrested cells. The ladder model results from traditional EM samples, which are vulnerable to fixation and staining artifacts. Furthermore, the ladder model was derived from projections through tens of nanometers of cell mass, which may obfuscate the structural details of thick macromolecular complexes (Fig. S3A). We tested this second possibility by comparing projection images of cryosections with the increasingly thick cryotomographic slices from the same positions. Indeed, if the triple-helices are not perfectly perpendicular to the cryosection plane, they appeared like filaments running parallel to the cryosection surface in the thickest tomographic slices (Fig. S3, B and C). Projections of this SC position have a chevron motif that

vaguely resembles a ladder and they illustrate how projection images can mask the details of the SC's underlying subunit structure.

The yeast SC has abundant triple-helices

Cryotomographic slices show two common motifs -- densely packed ~ 12-nm-wide filaments and trefoil-shaped densities that have a maximum width of ~ 12-nm (Fig. 4, A and B). When we examined sequential tomographic slices, the triple-helical filaments that were perpendicular to the cryosection surface appeared to "rotate", indicating that they are helical (Movie S1). To obtain a higher-resolution model of the SC filaments, we performed template matching, classification, and subtomogram averaging of SC subvolumes from all three strains studies here: DK428 treated with 5% 1,6-hexanediol (see below), NKY611, and EW104, which were incubated 4, 6, and 8 hours in SM, respectively. We treated the SC triple-helical filaments as sequential "single particle" segments, as is commonly done for single-particle analysis of helical structures (Egelman, 2010; Fromm and Sachse, 2016; He and Scheres, 2017). We template matched the SC segments with a 30-nm long by 12-nm diameter cylinder reference. To lower the chances of missing some SC segments, we used a very low cross-correlation cutoff. We removed false positives by 2-D classification, followed by 3-D classification (Fig. 4, C and D). All three strains yielded 3-D class averages of triple-helical SC segments. We 3-D refined the particles from the best 3-D classes.

We could not distinguish between the triple-helical filaments from the three strains at the current ~ 33 Å resolution. Note that the polarity of the helix cannot be resolved in the present data, which may contribute to the averages' moderate resolution. The 3-

D refined density maps showed that the triple helix is 12 nm thick (Fig. 4, D and E; Movies S1), with a rise of ~ 5 nm. We estimate the pitch to be ~ 130 nm. Each strand of the triple helix is ~ 5 nm thick. Our attempts to obtain averages of longer SC triple-helical filaments using a taller mask failed. Averages produced this way resembled featureless tubes, suggesting that the SC triple-helical filaments have variable curvature that negatively impacts the alignment process.

All three subtomogram averages revealed that the SC triple helix is right-handed. The handedness of electron tomograms is ambiguous unless a known chiral structure is imaged with the same conditions as the structure of interest (Briegel *et al.*, 2013). Ribosomes are omnipresent and have asymmetric features that are visible in *in situ* subtomogram averages (Pierson *et al.*, 2010; Cai *et al.*, 2018b). We therefore performed template matching, classification, and subtomogram averaging of cytoplasmic ribosomes from *ndt80*Δ cell cryotomograms, which had the highest contrast. One 80S ribosome class average shows that the characteristic “beak” motif is oriented in the direction expected of a ribosome (Fig. S4). This experiment confirms that the SC triple helix is right-handed.

The SC triple-helical filaments are sensitive to 1,6-hexanediol

An earlier study showed that 1,6-hexanediol can reversibly disperse yeast CR proteins, but not from their LEs (Rog *et al.*, 2017). We took advantage of this differential chemical sensitivity to distinguish CR from LE components in our cryotomograms. We incubated WT cells with 1,6-hexanediol for 1 minute and then imaged them by fluorescence microscopy. In the presence of 5% 1,6-hexanediol, the Zip1-GFP fluorescence signals appeared uniform in the nucleus while in 7% 1,6-

hexanediol, the Zip1-GFP signal was largely cytoplasmic (Fig. 5A). We then performed cryo-ET of WT cells with 0% (control), 5%, or 7% 1,6-hexanediol treatment (Fig. 5, B - D). Bundles of triple-helical filaments were present in untreated cells and in 5% 1,6-hexandediol-treated cells (Fig. 5, B and C). In the presence of 7% 1,6-hexanediol, cells did not have the bundles of triple-helical filaments. Instead, in some cells we observed bundles of thinner filaments (Fig. 5D). These experiments suggest that the majority of SC triple-helical filaments belong to the CR and they raise the possibility that the 1,6-hexanediol-resistant filaments may be LE components. We attempted subtomogram 3-D classification of these 1,6-hexanediol-resistant filaments but did not observed any meaningful class averages, either because these filaments are too conformationally heterogeneous or due to the limited contrast. We also cannot rule out that these thinner filaments are a different polymer of the triple-helix protein, which need 1,6-hexanediol.

SCs pack into crystalline bundles

SCs were recently proposed to be a form of biological liquid crystal (Rog *et al.*, 2017). To better characterize the SC's crystalline properties, we attempted to make 3-D models of bundles of triple-helical filaments. Because the remapping of subtomogram averages can reveal higher-order motifs in chromatin structure (Cai *et al.*, 2018a; Cai *et al.*, 2018c), we remapped the subtomogram averages of the SC triple helix segments back into the tomogram. This approach failed because the filaments appeared discontinuous; template matching and classification are imperfect, resulting in the removal of many SC triple helix segments. As an alternative, we manually modeled each SC triple helix as rod (Fig. 6, A and B). Note that due to missing-wedge effects, we could not model bundles of triple-helical

filaments running parallel to the cryosection surface. The 3-D models show that the triple-helical filaments form domains of largely parallel filaments. To better characterize the crystallinity of the SC, we generated power spectra by Fourier transforming the tomographic slices of the largest WT filament bundles (Fig. 6, C and D). These power spectra revealed broad peaks corresponding to spacings between 14 and 22 nm, consistent with hand-measured center-to-center distances between neighboring triple-helical filaments. These distances here reflect packing of helices, not the shorter characteristic distances seen in helical diffraction patterns. This tight packing is consistent with the absence of macromolecular complexes, such as nucleosome-like particles, in between the triple-helical filaments. The peaks appear elongated instead of circular, suggesting that each SC position has a narrow range of inter-helix spacings. To determine how much of the SC mass in a cell is crystalline, we attempted to reconstruct as much of a single cell as possible by serial Volta cryo-ET of cryosections. We successfully reconstructed six sequential sections from one *ndt80*Δ cell (Fig. S5). These reconstructions show that nearly all of the SC triple-helical filaments in a 420-nm-thick sample of the cell were tightly bundled into crystalline domains.

DISCUSSION

SC architecture visualized by cryo-ET

The SC has been extensively studied in many organisms ever since its discovery six decades ago (Fawcett, 1956; Moses, 1956). While the approximate positions of the SC components are known, the higher-resolution 3-D details have remained ambiguous. Our data shows that the yeast SC is a thick structure, consistent with both tomography of plastic sections of beetle SCs (Schmekel *et al.*, 1993) and with super-resolution 3-D analysis of the fly SC (Cahoon *et al.*, 2017). We are unable to distinguish layered structures in any of the cells we have imaged. Instead, the triple-helical filaments are tightly bundled, with little nucleoplasm in between. Chromatin is absent from the SC positions we captured in our cryotomograms. We also did not detect any dense aggregates of nucleosome-like particles in the SC's periphery. While we cannot rule out the presence of naked DNA mixed either within or peripheral to the SC's bundled triple-helical filaments, our data are mostly consistent with structured-illumination studies of yeast chromosome spreads (Voelkel-Meiman *et al.*, 2013).

Triple-helical filaments are the main subunits of the yeast SC

Our study has revealed that the SC is comprised of densely packed triple-helical protein complexes. The triple helix is approximately 12-nm thick at its widest point and has a 5-nm rise and a 130-nm pitch. Each of the three strands is approximately 5-nm thick. The center-to-center separation between SC triple-helix segments is variable, and ranges from 14 nm to at least 22 nm. In unperturbed cells, we have not detected single triple-helical filaments, single or double 5-nm-thick strands, or any

smaller oligomer that could be an assembly intermediate. The rarity of such these smaller assemblies suggests that the intra- and inter-triple-helix interactions are stable.

The budding-yeast TF protein Zip1 oligomerizes head-to-head, with N termini at the SC centerline and C termini at the LEs; Zip1 spans the approximately 100-nm width of the CR (Sym and Roeder, 1995; Dong and Roeder, 2000; Schucker *et al.*, 2015). Homologous TF proteins SYCP1 in mice, C(3)G in flies, and SYP1 in worms all adopt the same orientation (Liu *et al.*, 1996; Anderson *et al.*, 2005; Schild-Prüfert *et al.*, 2011). Sequence analysis and EM of C-terminally truncated Zip1 suggest that this protein assembles as dimers with 50-nm-long coiled-coil domain and a ~ 20-nm-long globular domain (Tung and Roeder, 1998; Dong and Roeder, 2000). Zip1 can also form tetramers and larger oligomers without the help of other SC proteins *in vitro* (Dong and Roeder, 2000). Furthermore, nearly full-length Zip1p can form the larger oligomers. While Zip1 is the best candidate for the SC triple-helical filaments observed here, some observations disagree. First, the filament's strands are ~ 5-nm thick, which is incompatible with their being two-helix coiled coils. Second, there is no evidence -- *in vitro* -- that Zip1 forms trimers. Therefore, we cannot determine if the triple-helical filaments are Zip1 oligomers or are uncharacterized SC proteins.

Our cryo-ET data do not reveal densities that can be clearly attributed to central-element protein complexes. Two known yeast central-element proteins, Ecm11 and Gcm2 (Voelkel-Meiman *et al.*, 2013), may form complexes are either too small or too skinny to be detected in our data. Our data could not definitively reveal which densities belong to the LEs, which flank the CR (Voelkel-Meiman *et al.*, 2013;

Voelkel-Meiman *et al.*, 2019). While treatment with high concentrations of 1,6-hexanediol leaves thinner protein filaments intact, there is insufficient evidence for their assignment as LE subunits. In the unperturbed cells, we observe many triple-helical filaments that are perpendicular to other bundles of triple-helical filaments. This observation implies that either a subset of CR proteins is oriented parallel to the LE or that at least one of the LE components may form triple-helical filaments.

Mechanical implications of liquid polycrystals

Meiotic chromosomes have mysterious properties that remain unexplained. One conserved property is called crossover interference, whereby the presence of a crossover lowers the probability of another crossover forming nearby in the same chromosome. This observation suggests that chromosomes can somehow transmit information along their lengths, and was once thought to be mediated by SCs (Sym and Roeder, 1994). The SC's role in crossover interference has been questioned (Börner *et al.*, 2004), leading to an alternative model in which chromosomes build up stress that is redistributed when a crossover forms. Our cryo-ET data nevertheless supports a model in which mechanical signal propagation is facilitated by the SC because its triple-helical filaments are packed so close. Alternatively, if the SC does not have the stiffness required to support this mechanical model, it may also transmit signals by acting as a one-dimensional conduit for signaling molecules that are "dissolved" within. These models were inspired by and consistent with the liquid-crystal framework that was recently explored for both worm and yeast SCs (Rog *et al.*, 2017).

Our observation of imperfectly packed triple-helical filaments gives hints about the SC's mechanical flexibility, i.e., how it can follow the sinuous path that homologous chromosomes trace through the nucleus. This phenomenon is most clearly seen when the SC is depicted as a ribbon (Byers and Goetsch, 1975; Hernandez-Hernandez *et al.*, 2016). Furthermore, the SC can accommodate extreme chromosome dynamics in living cells (White *et al.*, 2004; Rog and Dernburg, 2015). Our data reveals that the SC is polycrystalline, with imperfect packing within bundles of triple-helical filaments. The imperfect packing stems from both the curvature within each triple helix and the small defects between helices. We propose that the polycrystalline packing allows some triple-helical filaments to remain in contact regardless of the nature of the mechanical distortion (Fig. 7), thereby conferring mechanical stability and an unbroken end-to-end chromosomal communication "channel" throughout pachytene.

Conclusion

Our work is a starting point to better understand the structural cell-biology of other meiotic macromolecular complexes and events *in situ*. Higher-resolution analysis and deeper classification will potentially enable the construction of SC quasi-atomic models by docking in high-resolution structures of the SC's major subassemblies (Kim *et al.*, 2014; Lu *et al.*, 2014; Syrjanen *et al.*, 2014; Seo *et al.*, 2016; Dunce *et al.*, 2018; West *et al.*, 2019). Finally, our study raises questions about SC assembly and disassembly: do triple-helical filaments assemble first and then aggregate into the SC or do pre-bundled triple-helical filaments assemble onto paired meiotic chromosomes?

MATERIALS AND METHODS

Strains

Strains DK428 and EW104 used in this study were from the Kaback lab. Strain NKY611 was from the Surana lab. The haploid LY2 strain was from Lacefield lab. The key genotypic features are summarized in Table S1.

Cell culture and synchronization

Most experiments were done at at 23°C (room temperature) unless noted otherwise. Cells were sporulated using an established protocol (White *et al.*, 2004) as follows. A single colony from a YPD plate was inoculated into 3 ml YPD [1% yeast extract, 2% Bacto peptone, 2% D-glucose] medium and grown overnight at 30°C with shaking at 220 RPM in a 250 ml flask. Cells were pelleted at 3,000 × g for 5 minutes and then resuspended in 20 ml YPA (pre-sporulation) medium [0.5% yeast extract, 1% Bacto peptone, 1% potassium acetate]. After 3 hours incubation at 30°C, cells were pelleted, washed with ddH_2O (deionized and distilled water, > 18 MΩ·cm), and then resuspended in 20 ml sporulation medium (SM, 2% potassium acetate) with 0.5 ml amino acid supplement [0.04 g/L L-proline, 0.02 g/L L-lysine, 0.08 g/L L-tyrosine, 0.2 g/L L-histidine, 0.2 g/L L-leucine, 0.2 g/L L-methionine, 0.2 g/L L-tryptophan,0.2 g/L L-arginine, 0.4 g/L Adenine, 0.4 g/L Uracil, 1 g/L L-phenylalanine (Sigma # LAA21)]. Sporulation was carried out at 30°C with shaking.

Dissolution of Zip1 by 1,6-hexanediol

Six molar 1,6-hexanediol (Sigma # 88571) was diluted with ddH_2O to a final concentration of 10% or 14% (w/v). DK428 cells (1 ml) were incubated for 6 hours in

SM and then transferred to a 1.5 ml microfuge tube and centrifuged at 3,000 × g for 5 minutes. The cell pellet was resuspended with 0.5 ml ddH_2O. For 5% or 7% hexanediol treatment, 0.5 ml of 10% or 14% hexanediol solution was added to 0.5 ml of cell suspension and then mixed by pipetting for 1 minute. Fluorescence microscopy was performed on 4 µl of hexanediol-treated cell mixture that was spread onto a microscope slide.

Fluorescence microscopy

Sporulating cells were fixed with 3.7% formaldehyde in SM for 60 minutes at 30°C and then pelleted by centrifugation at 3,000 × g for 5 minutes. Three µl of cells were added to a microscope slide. For the fixed cells, the DNA was stained with Vectashield-DAPI (Vector Laboratories, Inc.). Images were recorded using a PerkinElmer Ultraview Vox spinning disc confocal microscope with a 100× oil-immersion objective lens.

Plastic sectioning

EW104 (*ndt80*Δ) cells were harvested after an 8-hour SM incubation and then fixed with 4% paraformaldehyde in SM for 1 hour at 30°C. The fixed cells were washed three times with water and then partially lysed with a yeast nuclei isolation kit (Abcam 206997) using the following modified protocol. The cell pellet was resuspended in 1 ml Buffer A (from the kit, with 10 mM dithiothreitol added), then incubated for 10 minutes in a 30°C water bath. Cells were pelleted at 1,500 × g for 5 minutes at 23°C and resuspended in 1 ml Buffer B (from the kit). After addition of 10 µl lysis enzyme cocktail (from the kit), the cells were incubated at 30°C for 15 minutes with shaking at 220 RPM and then pelleted at 1,500 × g at 4°C. The cell

pellet was resuspended in buffer C and incubated at 23°C for 10 minutes and then washed in ddH_2O. Plastic sections were prepared from this cell pellet using a published protocol (Schmekel, 2000) that was modified as follows. The partially lysed cells were dehydrated at 23°C with a series of treatments: 70% ethanol (20 minutes), 90% ethanol (20 minutes), 95% ethanol (20 minutes), 100% ethanol (20 minutes, twice), 50% ethanol: 50% LR White, Hard grade, London Resin Company (1 hour), 100% LR White (overnight). The cells were transferred into a gelatin capsule filled with LR White resin and then polymerized at 50°C for 24 hours. Plastic sections (80 nm nominal) were cut in a Leica Ultracut UCT/FCS with a glass knife, floated onto a water trough, collected with a 200 mesh EM grid, and stained with UranyLess (Electron Microscopy Sciences #22409) at 23°C for 1 hour. Projection images were collected with a Tecnai T12 transmission electron cryomicroscope (Thermo Fisher Scientific (TFS), Eindhoven, Netherlands).

Self-pressurized freezing and vitreous sectioning

Cells were self-pressurized frozen using a modified method from (Yakovlev and Downing, 2011). Sporulating cells were pelleted by centrifugation at 3,000 × g for 5 minutes at 23°C. The cell pellet was mixed with 60% dextran (M_r = 40 kDa, Sigma) in SM. The cell/dextran mixture was quick spun for 30 seconds to disrupt bubbles and then loaded into a copper tube (0.3 mm inner diameter) with a syringe-type filler device (part 733-1, Engineering Office M. Wohlwend GmbH). Both ends of the copper tube were tightly clamped with flat-nosed pliers and then dropped into liquid ethane. Before loading into the microtome, the tubes' clamped ends were cut off with a tube-cut device (Part. 732, Engineering Office M. Wohlwend GmbH) operated in liquid nitrogen.

EM grids were pre-coated with 4 µl of gold/BSA solution [0.1 mg/ml BSA with 10-nm gold fiducials (Sigma #G1527), in ddH_2O] and air dried for either 3 hours or overnight before use. Vitreous sections of 70 or 100 nm nominal thickness were cut with a diamond knife (Diatome, No. 16DIA.DCO3530, Nidau, Switzerland) in a Leica UC7/FC7 cryo ultramicrotome (Leica Microsystems, Vienna, Austria) operated at -150°C and augmented by dual micromanipulators (Ladinsky *et al.*, 2006; Studer *et al.*, 2014). The ribbon was attached to the gold pre-coated EM grid by charging with a Crion device (Leica Microsystems) in charge mode for 1 minute. The grid was stored in liquid nitrogen until imaging.

Electron cryotomography imaging and reconstruction

Tilt series were collected using Tomography 4 on a Titan Krios transmission electron cryomicroscope equipped with a Volta phase plate and a Falcon II direct-detection camera (all TFS). The detailed imaging parameters are listed in Table S2. Cryotomogram reconstruction was performed semi-automatically using the batch processing function of the IMOD software package (Kremer *et al.*, 1996; Mastronarde, 1997; Mastronarde and Held, 2017). No CTF compensation was done. All cryotomograms analyzed in this paper were deposited as EMPIAR-##### and are detailed in Table S3.

Template matching and initial model

All references were created with the Bsoft program *beditimg* (Heymann and Belnap, 2007), while masks were created with *beditimg* and the RELION (REgularised LIkelihood OptimisatioN) program *relion_mask_create* (Scheres, 2012). Uniformly

spaced search points were seeded with the PEET program *gridInit* (Particle Estimation for Electron Tomography) (Nicastro *et al.*, 2006; Heumann, 2016). Template matching was done using PEET. We used different template-matching strategies for SCs, nucleosome-like particles, and ribosomes. The details are listed in Table S4. SC filaments are long and curvy, so they needed to be treated as shorter helical segments. The grid points fit in a rectangular box that enclosed the bundles of triple-helical filaments. The search was done with 10° angular increments and using a Gaussian low-pass filter. To minimize the influence of nearby particles, the subtomograms were masked by a cylinder (SC triple helix and nucleosome) or sphere (ribosome) that was extended 1 - 2 nm beyond the reference's outer-most pixels. Only one round of template matching was done, i.e., the reference was not refined. To lower the number of false negatives, we used a very low cross-correlation cutoff of ~ 0.1 to 0.3. This criterion resulted in more than 10-fold excess of false positives, as assessed by comparing the number of hits that remained after the classification process described below.

Subtomogram classification

Subtomogram classification and averaging were performed using RELION's subtomogram-analysis routines (Bharat *et al.*, 2015; Kimanius *et al.*, 2016; Zivanov *et al.*, 2018). Two-dimensional classification of the projected subtomograms revealed class averages that clearly distinguished between the SC densities and globular structures (Bharat *et al.*, 2015). For 3-D classification, a 24-nm tall, 7-nm diameter cylindrical rod was used as a reference. To suppress the influence of neighboring particles, the densities were masked with a 16-nm tall, 19-nm-diameter soft-edged cylinder. No symmetry was enforced. Some of the resultant 3-D class averages were

triple-helical filaments, with the same width as the bundled filaments seen in the cryotomograms. Other 3-D class averages had poorly defined shapes. To improve the detection of false positives, the dimensions (length and radius) of the mask were varied. A taller cylindrical mask (24 nm) enabled the detection of rod-shaped densities that are shorter than the SC triple helix. This new mask also probably caused the removal of the template-matching hits of SC triple-helical filaments close to the cryosection surface, where cryosectioning artifacts and contaminants generate spurious densities. Two rounds of 3-D classification using this taller mask pruned the dataset to a few thousands subtomograms. These subtomograms were then subjected to 3-D autorefinement, but using a shorter, 16-nm-tall mask. Use of the shorter mask resulted in class averages that have higher-resolution features, such as 5-nm periodic density bumps along the helical axis. These features were absent when taller masks were used probably because the SC filaments have variable curvatures. The resultant higher signal-to-noise-ratio class average allowed us to more accurately measure the diameters and design a new, shorter cylindrical template. Furthermore, this shorter class average (and correspondingly shorter cylindrical mask) was used for a second round of template matching, but with a denser search grid to maximize the number of SC triple-helical filament-containing subtomograms detected. The second set of template-matching hits was filtered at a cross-correlation coefficient cutoff of 0.2. This cutoff was determined subjectively by incremental increases, followed by inspection of the hit positions in the cryotomograms. The cutoff was chosen such that a nearly equal number of obvious nucleoplasmic false positives, such as nucleosome-like particles, were also included. These hits were subjected to 2-D and 3-D classification again.

Three-dimensional refinement was done using 841, 1513, and 4456 triple-helix segments from NKY611, DK428, and EW104 cells, respectively. Preliminary 3-D refinement on EW104 SC triple helix segments produced a Fourier shell correlation curve that did not drop to zero in the highest-resolution range. This artifact was caused by new "duplicate" particles that were generated by the 3-D classification translational search (Cai *et al.*, 2018a). These new duplicates were removed by re-running template matching with PEET, using only the coordinates of the 3-D classified particles. The remaining 4161 SC segments were re-refined in RELION.

Fourier analysis

To maximize the signal-to-noise ratio, SC positions with the largest bundles of triple-helices were selected. Tomographic slices (10 nm) were exported as TIFF files and read into FIJI v2.0.0 (Schindelin *et al.*, 2012). A ~512-pixel-wide rectangular selection was made around the SC position and then Fourier transformed using the FFT tool. The distance d*, in inverse pixels, between a peak's center of mass and the origin was measured using the straight-line tool. This distance was converted to real space units with the equation

$$d = 512 \times pixel / d^*$$

The "pixel" value was the real-space pixel size (0.58 nm).

Data sharing

A representative late-prophase cell Volta cryotomogram (Strain NKY611, frozen after 4 hours in SM) has been deposited as EMDB as entry EMD-####. This cryotomogram, along with the tilt series for all cryotomograms analyzed in this paper

(Table S2) were deposited in EMPIAR (Iudin *et al.*, 2016) as entry EMPIAR-#####. Data that was collected for this study but not analyzed, i.e., “surplus” tilt series and tomograms, will be deposited in EMPIAR-10227 (Gan *et al.*, 2019).

Contributions

OXM - experiments, project design, writing; SC - training; JS - training; LG - experiments, project design, writing.

ACKNOWLEDGEMENTS

We thank the CBIS microscopy staff for support and training. We thank Soni Lacefield, Uttam Surana, and David Kaback for sharing strains and for their advice. OXM, SC, and LG were supported by a Ministry of Education Tier 1 grants R-154-000-A49-114 and R-154-000-B42-114 and Tier 2 grant R-154-100-B58-112.

REFERENCES

Anderson, L.K., Royer, S.M., Page, S.L., McKim, K.S., Lai, A., Lilly, M.A., and Hawley, R.S. (2005). Juxtaposition of C(2)M and the transverse filament protein C(3)G within the central region of Drosophila synaptonemal complex. Proc Natl Acad Sci U S A *102*, 4482-4487.

Bharat, T.A., Russo, C.J., Lowe, J., Passmore, L.A., and Scheres, S.H. (2015). Advances in Single-Particle Electron Cryomicroscopy Structure Determination applied to Sub-tomogram Averaging. Structure *23*, 1743-1753.

Bhuiyan, H., Dahlfors, G., and Schmekel, K. (2003). Lateral elements inside synaptonemal complex-like polycomplexes in ndt80 mutants of yeast bind DNA. Genetics *163*, 539-544.

Bollschweiler, D., Radu, L., Plitzko, J.M., Henderson, R.M., Mela, I., and Pellegrini, L. (2018). Reconstitution of a flexible SYCP3-DNA fibre suggests a mechanism for SYCP3 coating of the meiotic chromosome axis. bioRxiv.

Börner, G.V., Kleckner, N., and Hunter, N. (2004). Crossover/noncrossover differentiation, synaptonemal complex formation, and regulatory surveillance at the leptotene/zygotene transition of meiosis. Cell *117*, 29-45.

Briegel, A., Pilhofer, M., Mastronarde, D.N., and Jensen, G.J. (2013). The challenge of determining handedness in electron tomography and the use of DNA origami gold nanoparticle helices as molecular standards. J Struct Biol *183*, 95-98.

Byers, B., and Goetsch, L. (1975). Electron microscopic observations on the meiotic karyotype of diploid and tetraploid Saccharomyces cerevisiae. Proc Natl Acad Sci U S A *72*, 5056-5060.

Cahoon, C.K., Yu, Z., Wang, Y., Guo, F., Unruh, J.R., Slaughter, B.D., and Hawley, R.S. (2017). Superresolution expansion microscopy reveals the three-dimensional organization of the Drosophila synaptonemal complex. Proc Natl Acad Sci U S A *114*, E6857-E6866.

Cai, S., Böck, D., Pilhofer, M., and Gan, L. (2018a). The in situ structures of mono-, di-, and trinucleosomes in human heterochromatin. Mol Biol Cell *29*, 2450-2457.

Cai, S., Chen, C., Tan, Z.Y., Huang, Y., Shi, J., and Gan, L. (2018b). Cryo-ET reveals the macromolecular reorganization of S. pombe mitotic chromosomes in vivo. Proc Natl Acad Sci U S A *115*, 10977-10982.

Cai, S., Song, Y., Chen, C., Shi, J., and Gan, L. (2018c). Natural chromatin is heterogeneous and self-associates in vitro. Mol Biol Cell *29*, 1652-1663.

Carpenter, A.T. (1975). Electron microscopy of meiosis in Drosophila melanogaster females. I. Structure, arrangement, and temporal change of the synaptonemal complex in wild-type. Chromosoma *51*, 157-182.

Chen, C., Lim, H.H., Shi, J., Tamura, S., Maeshima, K., Surana, U., and Gan, L. (2016). Budding yeast chromatin is dispersed in a crowded nucleoplasm in vivo. Mol Biol Cell *27*, 3357-3368.

Chu, S., and Herskowitz, I. (1998). Gametogenesis in yeast is regulated by a transcriptional cascade dependent on Ndt80. Mol Cell *1*, 685-696.

Dong, H., and Roeder, G.S. (2000). Organization of the yeast Zip1 protein within the central region of the synaptonemal complex. J Cell Biol *148*, 417-426.

Dunce, J.M., Dunne, O.M., Ratcliff, M., Millan, C., Madgwick, S., Uson, I., and Davies, O.R. (2018). Structural basis of meiotic chromosome synapsis through SYCP1 self-assembly. Nat Struct Mol Biol *25*, 557-569.

Egelman, E.H. (2010). Reconstruction of helical filaments and tubes. Methods Enzymol *482*, 167-183.

Eltsov, M., Grewe, D., Lemercier, N., Frangakis, A., Livolant, F., and Leforestier, A. (2018). Nucleosome conformational variability in solution and in interphase nuclei evidenced by cryo-electron microscopy of vitreous sections. Nucleic Acids Res *46*, 9189-9200.

Fawcett, D.W. (1956). The fine structure of chromosomes in the meiotic prophase of vertebrate spermatocytes. J Biophys Biochem Cytol *2*, 403-406.

Fromm, S.A., and Sachse, C. (2016). Cryo-EM Structure Determination Using Segmented Helical Image Reconstruction. Methods Enzymol *579*, 307-328.

Fukuda, Y., Laugks, U., Lucic, V., Baumeister, W., and Danev, R. (2015). Electron cryotomography of vitrified cells with a Volta phase plate. J Struct Biol *190*, 143-154.

Gan, L., and Jensen, G.J. (2012). Electron tomography of cells. Quart. Rev. Biophys. *45*, 27-56.

Gan, L., Ng, C.T., Chen, C., and Cai, S. (2019). A collection of yeast cellular electron cryotomography data. Gigascience *8*.

Gladstone, M.N., Obeso, D., Chuong, H., and Dawson, D.S. (2009). The synaptonemal complex protein Zip1 promotes bi-orientation of centromeres at meiosis I. PLoS Genet *5*, e1000771.

He, S., and Scheres, S.H.W. (2017). Helical reconstruction in RELION. J Struct Biol *198*, 163-176.

Hernandez-Hernandez, A., Masich, S., Fukuda, T., Kouznetsova, A., Sandin, S., Daneholt, B., and Hoog, C. (2016). The central element of the synaptonemal complex in mice is organized as a bilayered junction structure. J Cell Sci *129*, 2239-2249.

Heumann, J.M. (2016). PEET: University of Colorado Boulder.

Heymann, J.B., and Belnap, D.M. (2007). Bsoft: image processing and molecular modeling for electron microscopy. J Struct Biol *157*, 3-18.

Iudin, A., Korir, P.K., Salavert-Torres, J., Kleywegt, G.J., and Patwardhan, A. (2016). EMPIAR: a public archive for raw electron microscopy image data. Nature methods *13*, 387-388.

Kane, S.M., and Roth, R. (1974). Carbohydrate metabolism during ascospore development in yeast. J Bacteriol *118*, 8-14.

Kim, Y., Rosenberg, S.C., Kugel, C.L., Kostow, N., Rog, O., Davydov, V., Su, T.Y., Dernburg, A.F., and Corbett, K.D. (2014). The chromosome axis controls meiotic events through a hierarchical assembly of HORMA domain proteins. Dev Cell *31*, 487-502.

Kimanius, D., Forsberg, B.O., Scheres, S.H., and Lindahl, E. (2016). Accelerated cryo-EM structure determination with parallelisation using GPUs in RELION-2. Elife *5*.

Klein, F., Mahr, P., Galova, M., Buonomo, S.B., Michaelis, C., Nairz, K., and Nasmyth, K. (1999). A central role for cohesins in sister chromatid cohesion, formation of axial elements, and recombination during yeast meiosis. Cell *98*, 91-103.

Kremer, J.R., Mastronarde, D.N., and McIntosh, J.R. (1996). Computer visualization of three-dimensional image data using IMOD. J Struct Biol *116*, 71-76.

Ladinsky, M.S., Pierson, J.M., and McIntosh, J.R. (2006). Vitreous cryo-sectioning of cells facilitated by a micromanipulator. J Microsc *224*, 129-134.

Liu, J.G., Yuan, L., Brundell, E., Bjorkroth, B., Daneholt, B., and Hoog, C. (1996). Localization of the N-terminus of SCP1 to the central element of the synaptonemal complex and evidence for direct interactions between the N-termini of SCP1 molecules organized head-to-head. Exp Cell Res *226*, 11-19.

Lu, J., Gu, Y., Feng, J., Zhou, W., Yang, X., and Shen, Y. (2014). Structural insight into the central element assembly of the synaptonemal complex. Sci Rep *4*, 7059.

Macqueen, A.J., and Roeder, G.S. (2009). Fpr3 and Zip3 ensure that initiation of meiotic recombination precedes chromosome synapsis in budding yeast. Curr Biol *19*, 1519-1526.

Marini, G., Nueske, E., Leng, W., Alberti, S., and Pigino, G. (2018). Adaptive reorganization of the cytoplasm upon stress in budding yeast. bioRxiv.

Mastronarde, D.N. (1997). Dual-axis tomography: an approach with alignment methods that preserve resolution. J Struct Biol *120*, 343-352.

Mastronarde, D.N., and Held, S.R. (2017). Automated tilt series alignment and tomographic reconstruction in IMOD. J Struct Biol *197*, 102-113.

Moses, M.J. (1956). Chromosomal structures in crayfish spermatocytes. J Biophys Biochem Cytol *2*, 215-218.

Ng, C.T., Deng, L., Chen, C., Lim, H.H., Shi, J., Surana, U., and Gan, L. (2019). Electron cryotomography analysis of Dam1C/DASH at the kinetochore-spindle interface in situ. J Cell Biol *218*, 455–473.

Nicastro, D., Schwartz, C., Pierson, J., Gaudette, R., Porter, M.E., and McIntosh, J.R. (2006). The molecular architecture of axonemes revealed by cryoelectron tomography. Science *313*, 944-948.

Nueske, E., Marini, G., Richter, D., Leng, W., Bogdanova, A., Franzmann, T.M., Pigino, G., and Alberti, S. (2018). Filament formation by the translation factor eIF2B regulates protein synthesis in starved cells. bioRxiv.

Padmore, R., Cao, L., and Kleckner, N. (1991). Temporal comparison of recombination and synaptonemal complex formation during meiosis in S. cerevisiae. Cell *66*, 1239-1256.

Page, S.L., and Hawley, R.S. (2004). The genetics and molecular biology of the synaptonemal complex. Annu Rev Cell Dev Biol *20*, 525-558.

Pierson, J., Fernandez, J.J., Bos, E., Amini, S., Gnaegi, H., Vos, M., Bel, B., Adolfsen, F., Carrascosa, J.L., and Peters, P.J. (2010). Improving the technique of vitreous cryo-sectioning for cryo-electron tomography: electrostatic charging for section attachment and implementation of an anti-contamination glove box. J Struct Biol *169*, 219-225.

Rog, O., and Dernburg, A.F. (2015). Direct Visualization Reveals Kinetics of Meiotic Chromosome Synapsis. Cell Rep *10*, 1639-1645.

Rog, O., Kohler, S., and Dernburg, A.F. (2017). The synaptonemal complex has liquid crystalline properties and spatially regulates meiotic recombination factors. Elife *6*.

Scheres, S.H. (2012). RELION: implementation of a Bayesian approach to cryo-EM structure determination. J Struct Biol *180*, 519-530.

Scherthan, H., Wang, H., Adelfalk, C., White, E.J., Cowan, C., Cande, W.Z., and Kaback, D.B. (2007). Chromosome mobility during meiotic prophase in Saccharomyces cerevisiae. Proc Natl Acad Sci U S A *104*, 16934-16939.

Schild-Prüfert, K., Saito, T.T., Smolikov, S., Gu, Y., Hincapie, M., Hill, D.E., Vidal, M., McDonald, K., and Colaiacovo, M.P. (2011). Organization of the synaptonemal complex during meiosis in Caenorhabditis elegans. Genetics *189*, 411-421.

Schindelin, J., Arganda-Carreras, I., Frise, E., Kaynig, V., Longair, M., Pietzsch, T., Preibisch, S., Rueden, C., Saalfeld, S., Schmid, B., Tinevez, J.Y., White, D.J., Hartenstein, V., Eliceiri, K., Tomancak, P., and Cardona, A. (2012). Fiji: an open-source platform for biological-image analysis. Nature methods *9*, 676-682.

Schmekel, K. (2000). Methods for immunoelectron microscopic and fine structural analysis of synaptonemal complexes and nodules in yeast. Chromosoma *109*, 110-116.

Schmekel, K., and Daneholt, B. (1995). The central region of the synaptonemal complex revealed in three dimensions. Trends Cell Biol *5*, 239-242.

Schmekel, K., Wahrman, J., Skoglund, U., and Daneholt, B. (1993). The central region of the synaptonemal complex in Blaps cribrosa studied by electron microscope tomography. Chromosoma *102*, 669-681.

Schucker, K., Holm, T., Franke, C., Sauer, M., and Benavente, R. (2015). Elucidation of synaptonemal complex organization by super-resolution imaging with isotropic resolution. Proc Natl Acad Sci U S A *112*, 2029-2033.

Seo, E.K., Choi, J.Y., Jeong, J.H., Kim, Y.G., and Park, H.H. (2016). Crystal Structure of C-Terminal Coiled-Coil Domain of SYCP1 Reveals Non-Canonical Anti-Parallel Dimeric Structure of Transverse Filament at the Synaptonemal Complex. PLoS One *11*, e0161379.

Smith, A.V., and Roeder, G.S. (1997). The yeast Red1 protein localizes to the cores of meiotic chromosomes. J Cell Biol *136*, 957-967.

Spindler, M.-C., Filbeck, S., Stigloher, C., and Benavente, R. (2019). Quantitative basis of meiotic chromosome synapsis analyzed by electron tomography. bioRxiv.

Studer, D., Klein, A., Iacovache, I., Gnaegi, H., and Zuber, B. (2014). A new tool based on two micromanipulators facilitates the handling of ultrathin cryosection ribbons. J Struct Biol *185*, 125-128.

Sym, M., Engebrecht, J.A., and Roeder, G.S. (1993). ZIP1 is a synaptonemal complex protein required for meiotic chromosome synapsis. Cell *72*, 365-378.

Sym, M., and Roeder, G.S. (1994). Crossover interference is abolished in the absence of a synaptonemal complex protein. Cell *79*, 283-292.

Sym, M., and Roeder, G.S. (1995). Zip1-induced changes in synaptonemal complex structure and polycomplex assembly. J Cell Biol *128*, 455-466.

Syrjanen, J.L., Pellegrini, L., and Davies, O.R. (2014). A molecular model for the role of SYCP3 in meiotic chromosome organisation. Elife *3*.

Tung, K.S., and Roeder, G.S. (1998). Meiotic chromosome morphology and behavior in zip1 mutants of Saccharomyces cerevisiae. Genetics *149*, 817-832.

Voelkel-Meiman, K., Cheng, S.Y., Parziale, M., Morehouse, S.J., Feil, A., Davies, O.R., de Muyt, A., Borde, V., and MacQueen, A.J. (2019). Crossover recombination and synapsis are linked by adjacent regions within the N terminus of the Zip1 synaptonemal complex protein. PLoS Genet *15*, e1008201.

Voelkel-Meiman, K., Moustafa, S.S., Lefrancois, P., Villeneuve, A.M., and MacQueen, A.J. (2012). Full-length synaptonemal complex grows continuously during meiotic prophase in budding yeast. PLoS Genet *8*, e1002993.

Voelkel-Meiman, K., Taylor, L.F., Mukherjee, P., Humphryes, N., Tsubouchi, H., and Macqueen, A.J. (2013). SUMO localizes to the central element of synaptonemal complex and is required for the full synapsis of meiotic chromosomes in budding yeast. PLoS Genet *9*, e1003837.

West, A.M., Rosenberg, S.C., Ur, S.N., Lehmer, M.K., Ye, Q., Hagemann, G., Caballero, I., Uson, I., MacQueen, A.J., Herzog, F., and Corbett, K.D. (2019). A conserved filamentous assembly underlies the structure of the meiotic chromosome axis. Elife *8*.

White, E.J., Cowan, C., Cande, W.Z., and Kaback, D.B. (2004). In vivo analysis of synaptonemal complex formation during yeast meiosis. Genetics *167*, 51-63.

Xu, L., Ajimura, M., Padmore, R., Klein, C., and Kleckner, N. (1995). NDT80, a meiosis-specific gene required for exit from pachytene in Saccharomyces cerevisiae. Mol Cell Biol *15*, 6572-6581.

Yakovlev, S., and Downing, K.H. (2011). Freezing in sealed capillaries for preparation of frozen hydratedsections. J Microsc *244*, 235-247.

Zhang, L., Liang, Z., Hutchinson, J., and Kleckner, N. (2014). Crossover patterning by the beam-film model: analysis and implications. PLoS Genet *10*, e1004042.

Zickler, D., and Kleckner, N. (1999). Meiotic chromosomes: integrating structure and function. Annu Rev Genet *33*, 603-754.

Zickler, D., and Kleckner, N. (2015). Recombination, Pairing, and Synapsis of Homologs during Meiosis. Cold Spring Harb Perspect Biol *7*.

Zickler, D., and Olson, L.W. (1975). The synaptonemal complex and the spindle plaque during meiosis in yeast. Chromosoma *50*, 1-23.

Zivanov, J., Nakane, T., Forsberg, B.O., Kimanius, D., Hagen, W.J., Lindahl, E., and Scheres, S.H. (2018). New tools for automated high-resolution cryo-EM structure determination in RELION-3. Elife *7*.

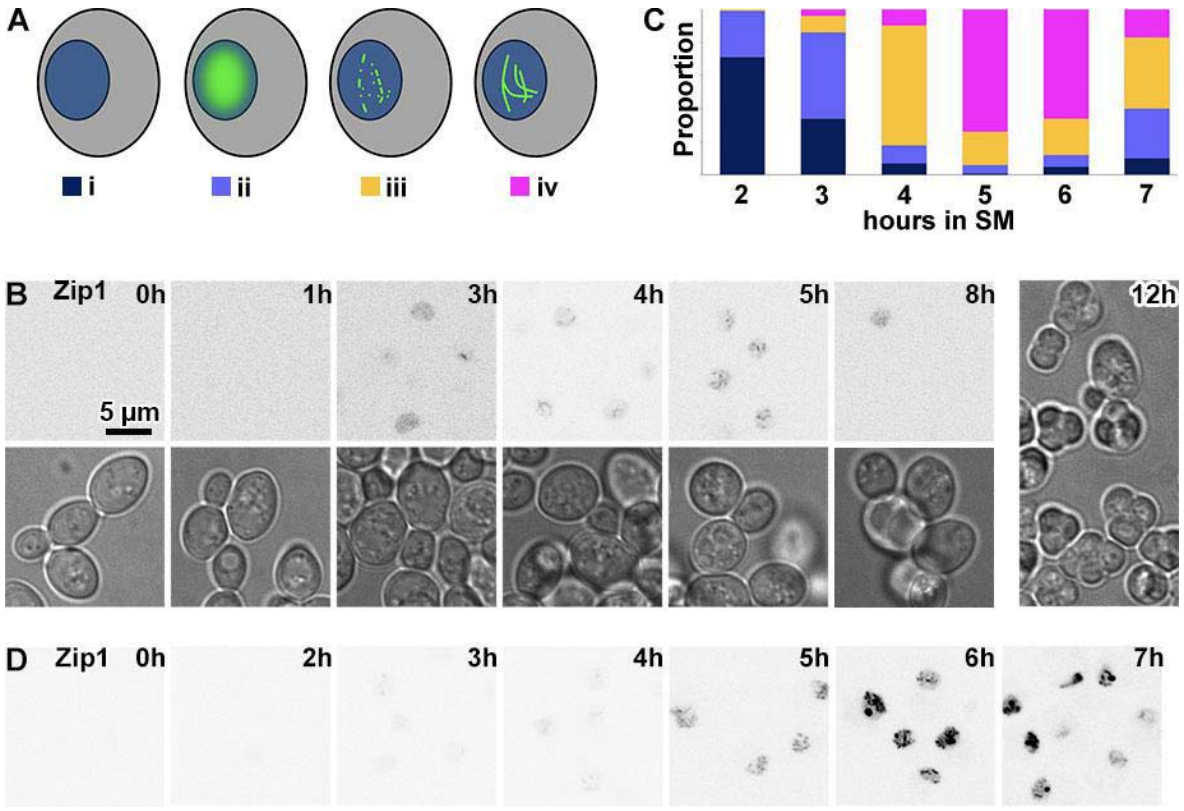

Figure 1. The assembly of the SCs monitored by Zip1-GFP.

(A) Cartoon of the different classes of Zip1-GFP fluorescence in meiotic prophase. i, nonfluorescent; ii, diffused fluorescence; iii, punctate fluorescence; iv, string-like fluorescence corresponding to full-length SCs. The nucleus is blue and the Zip1-GFP signal is green. This schematic in based on {White, 2004}. (B) WT cells expressing Zip1-GFP were withdrawn from liquid culture and imaged by fluorescence microscopy nearly every hour. Diffuse fluorescence started to appear after 2 hours and became punctate between 3 and 4 hours. Long linear SCs appeared after 5 hours in SM and became rarer after 7 hours. The right-most brightfield image shows WT cells after 12 hours in SM. Each ascus contained four spores. (C) Time course for SC formation in WT cells based on the Zip1-GFP fluorescence pattern. Approximately 100 cells were sampled at each time point. The color scheme is indicated under each cartoon in panel A. (D) Time course of *ndt80*Δ cells incubated in SM. The signal is from Zip1-GFP.

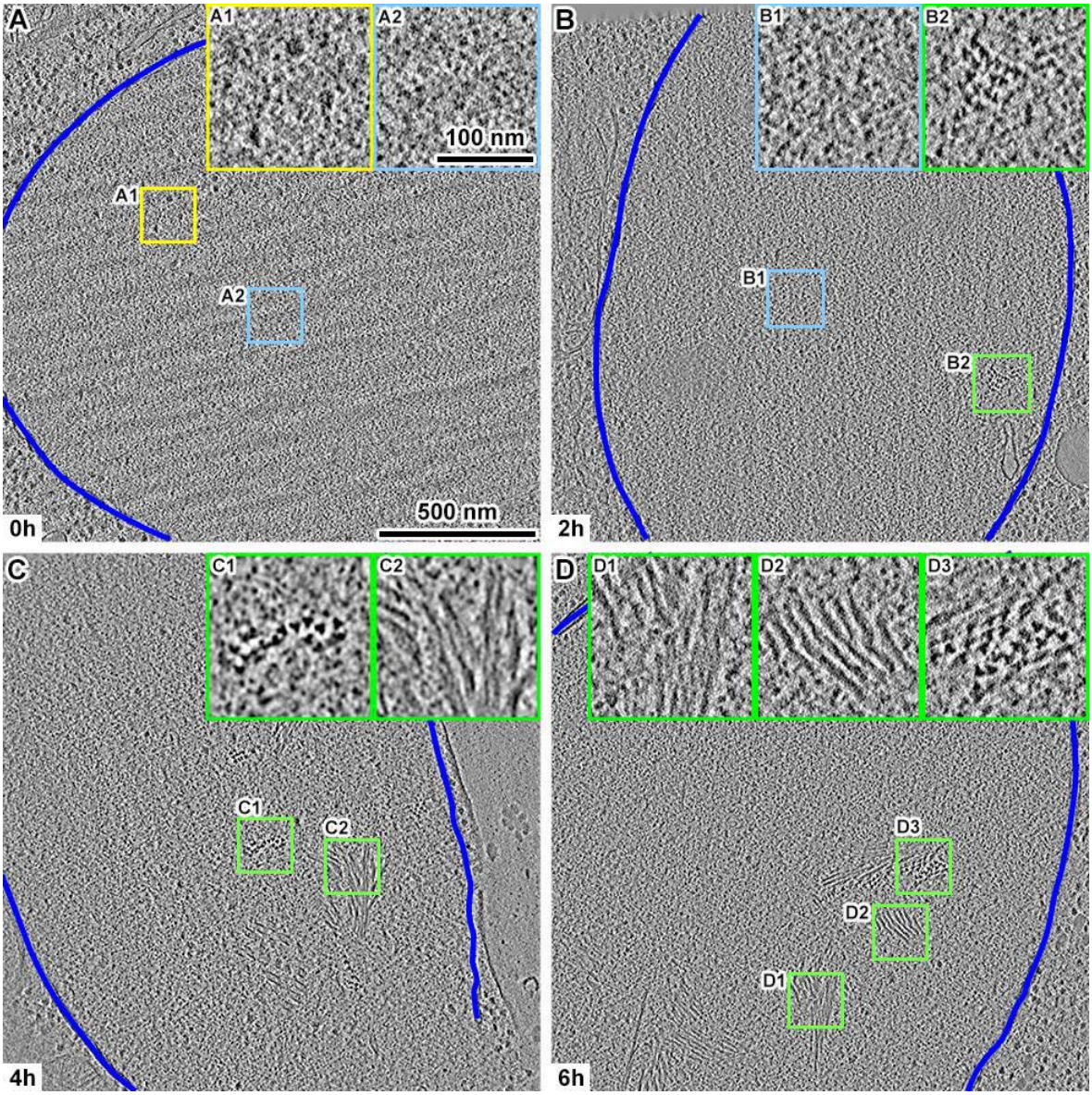

Figure 2. Visualization of SC assembly using cryo-ET.

Volta cryotomographic slices (10 nm) of WT cell nuclei (A) before meiosis and after (B) 2 hours, (C) 4 hours, and (D) 6 hours in SM. The boxed areas are enlarged 3-fold in the corresponding insets. Inset A1 shows 3 megacomplexes in the nucleolus. Insets A2 and B1 show nucleosome-like particles. Insets B2, C1, and D3 show clusters of SC filaments presenting a trefoil motif. Insets C2, D1, and D2 show bundles of SC filament proteins. The nuclear envelopes are delineated with the dark blue lines.

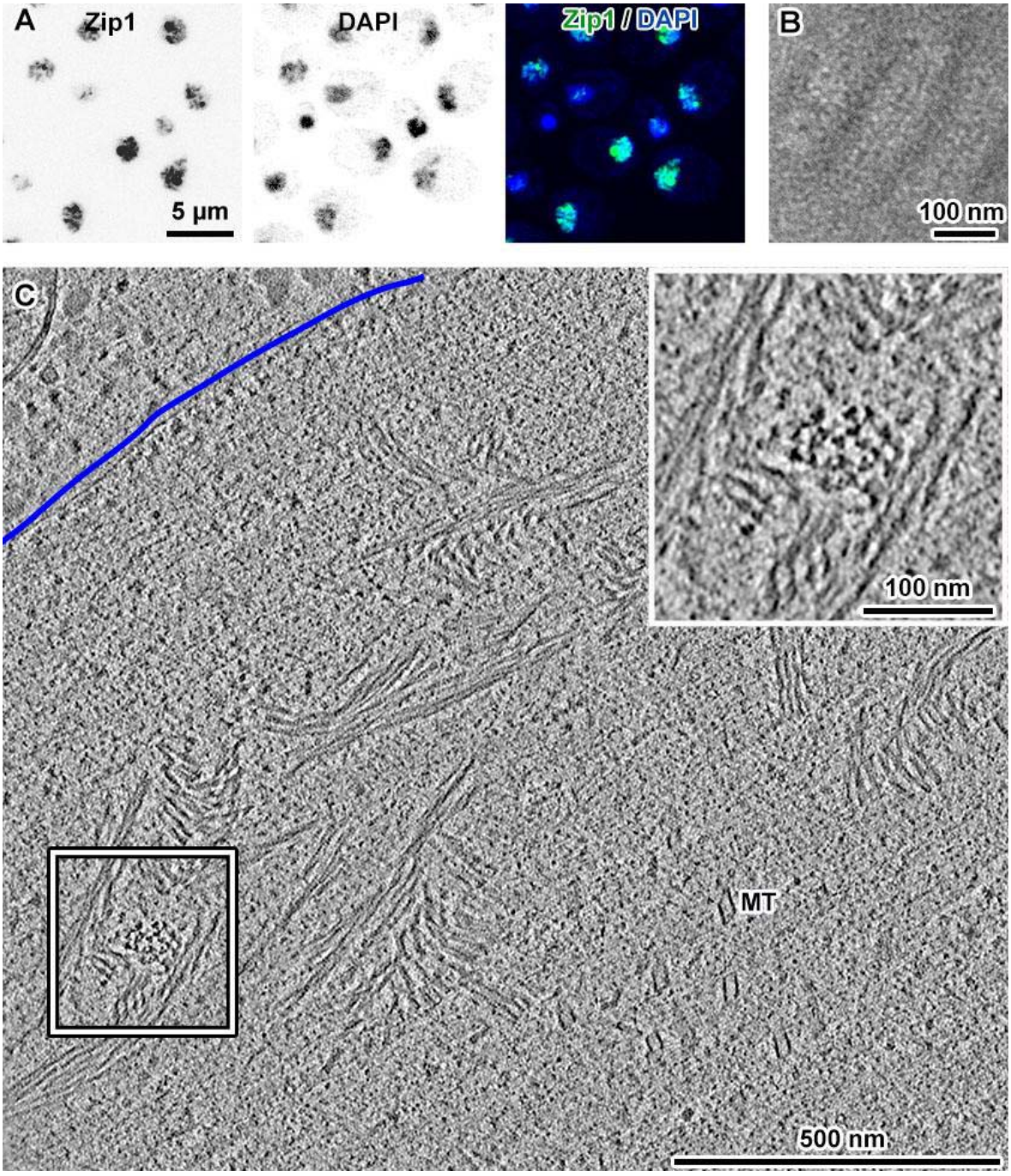

Figure 3. Pachytene-arrested cells are highly enriched in SC filaments.
(A) Fluorescence micrographs of pachytene-arrested *ndt80Δ* cells, after 8 hours in SM. Zip1-GFP fluorescence is found at both SCs (weak fluorescence) and polycomplexes (large, bright fluorescent bodies). The chromatin is stained by DAPI. Note that the polycomplex is poorly co-localized with the chromatin. (B) Plastic section showing a portion of a polycomplex in a pachytene-arrested *ndt80Δ* cell. (C) Volta cryotomographic 70-nm slice of the cryosection of a *ndt80Δ* cell at 8 hours in SM. The nuclear envelope (NE) is indicated by the blue line. The boxed area is enlarged 2-fold in the inset.

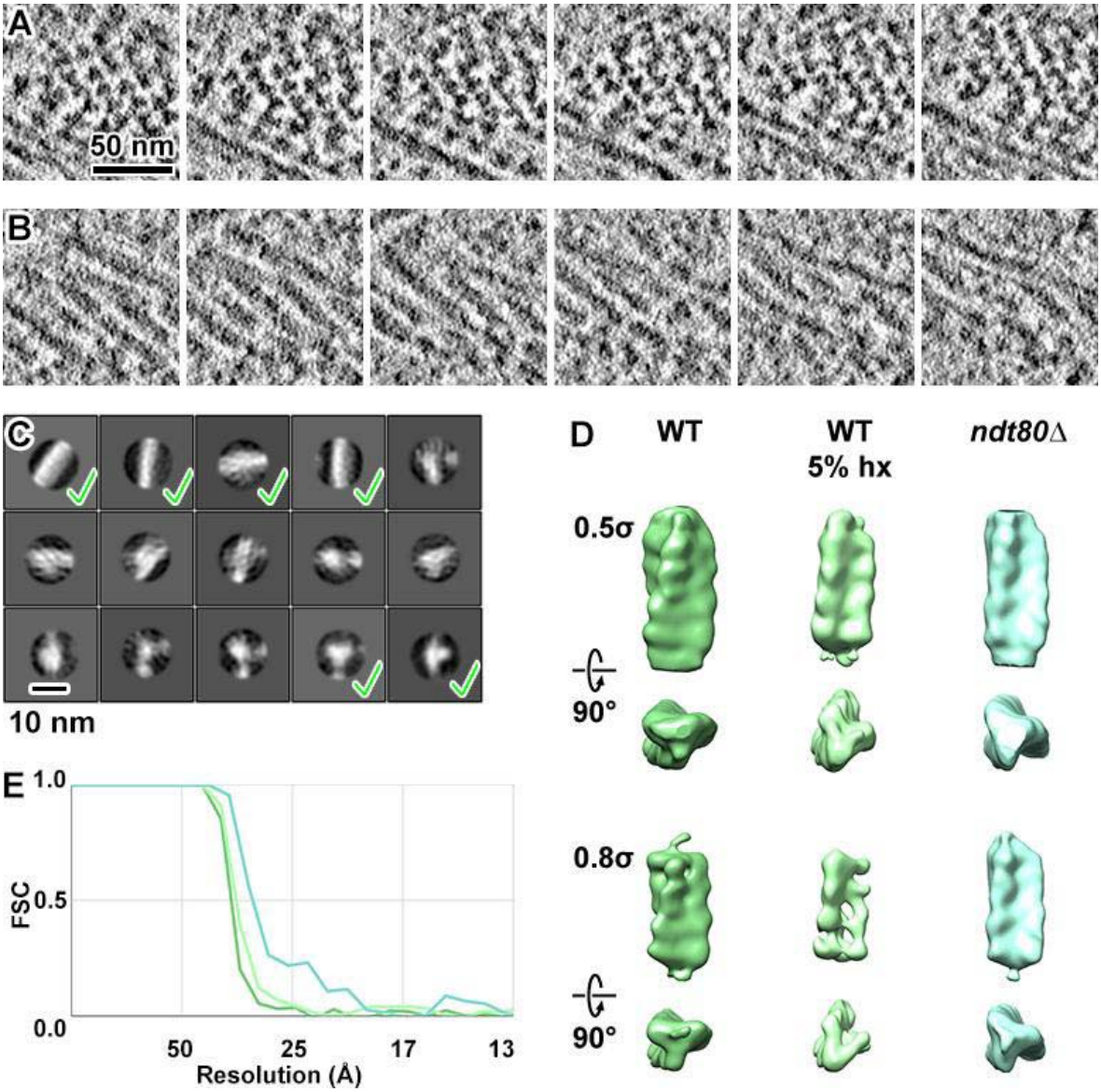

Figure 4. The yeast SC has densely packed protein triple-helical filaments

(A and B) Sequential Volta cryotomographic slices (12 nm) through bundles of SC subunits that have a trefoil and filamentous motif, respectively. (C) Class averages (2-D) of template-matched candidate SC filaments segments, taken from subvolumes within *ndt80*Δ pachytene-arrested cells. The class averages corresponding to triple-helical filaments are indicated by a green check mark and used for subsequent analysis. (D) Refined 3-D density map of SC triple helix segments from WT, WT treated with 5% 1,6-hexanediol, and *ndt80*Δ cells. They are rendered at two contour levels (0.5 σ and 0.8 σ) and viewed both perpendicular to (upper subpanels) and along (lower subpanels) the helical axis. (E) Fourier-shell correlation (FSC) plots of the triple helix segments from three conditions, color-coded similarly to panel B. The resolutions of the averages are ~ 33 Å, based on the "Gold standard" FSC = 0.5 criterion.

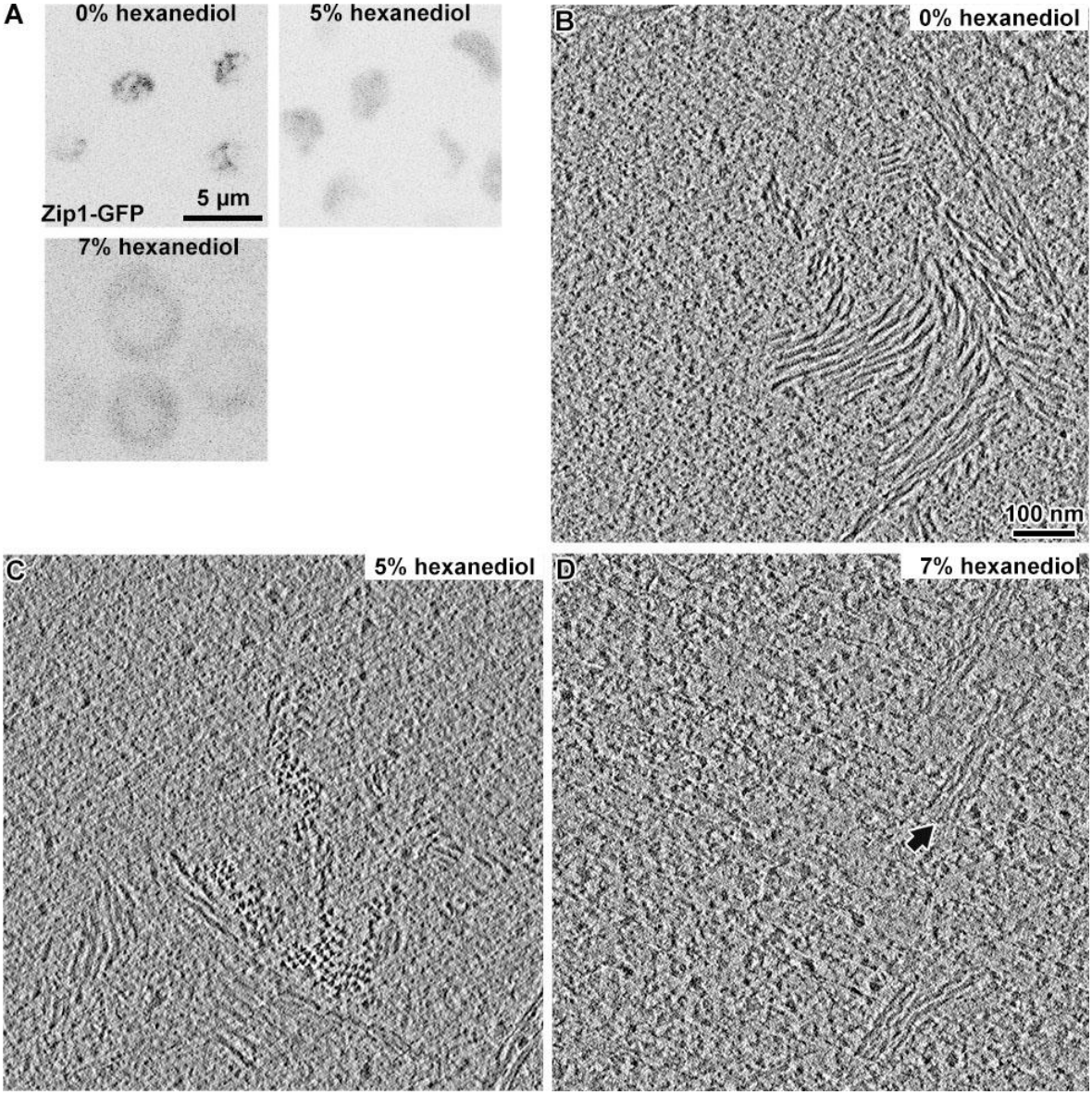

Figure 5. The SC triple helix may be a central-region complex

(A) GFP-fluorescence micrographs of WT cells treated with increasing concentrations of 1,6-hexanediol. The cells were harvested after 6 hours in SM and resuspended in SM (0% 1,6-hexanediol), or with 5% or 7% 1,6-hexanediol. In the lower subpanel, the light-gray oval in the middle of the cell is the nucleus; most of the Zip1-GFP signal (dark pixels) is cytoplasmic. (B) Volta cryotomographic slice (10 nm) of a WT cell in SM, showing bundles of SC triple-helical filaments. (C) Volta cryotomographic slice (10 nm) of a WT cell in 5% 1,6-hexanediol. This cell contains a few bundles of triple-helical filaments. Approximately half the tomograms of such cells (21 of 43) contain these bundles. (D) Volta cryotomographic slice (10 nm) of a WT cell in 7% 1,6-hexanediol. The arrow indicates a bundle of filaments of unknown structure.

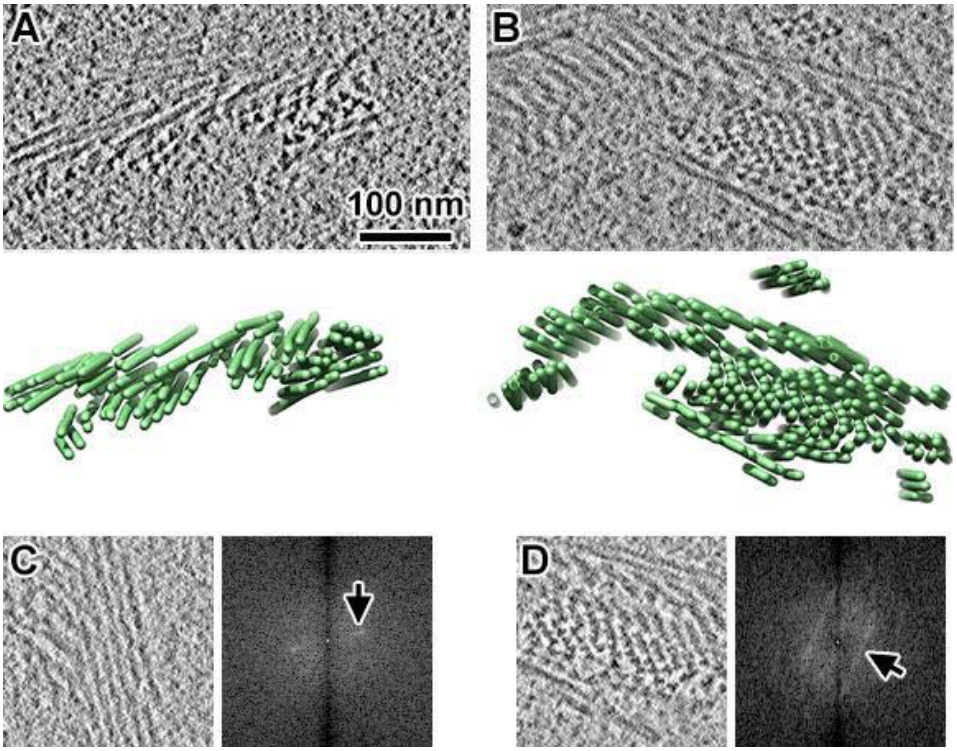

Figure 6. Yeast SCs have polycrystals

(A and B) Upper subpanels: Volta cryotomographic slices (10 nm) of WT cells that were frozen after a 4-hour incubation in SM. Lower subpanels: 3-D models of the distribution of SC filaments. Each filament is a triple helix, but is rendered as a tube. (C and D) Volta cryotomographic slices (left, 10 nm) and power spectra (right), taken at regions with many SC filaments. Panel D shows the same SC as panel B, but from a different position along the Z axis. Arrows point to broad peaks in the power spectra, which correspond to (C) 14 nm and (D) 22 nm spacings.

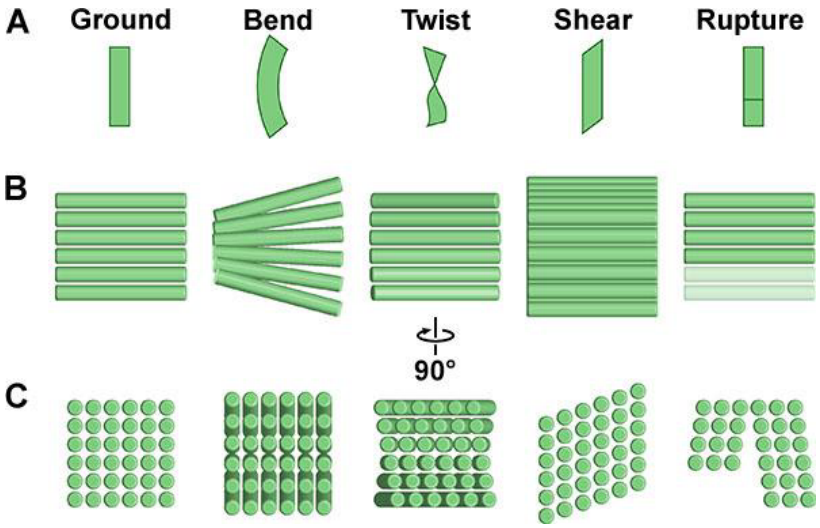

Figure 7. The SC is robust to mechanical perturbation

(A) Schematics of the crystalline SC and its distortions inside cells. In all the examples shown here, the chromosome axis is in the vertical direction. (B) Cartoon of a bundle of triple-helical filaments (each represented by a rod) within an SC that is distorted in the configuration shown by the same column in panel A. (C) The corresponding SC configurations, viewed from the "side" of the SC. For clarity, the filament packing is depicted with more order than in the cell.

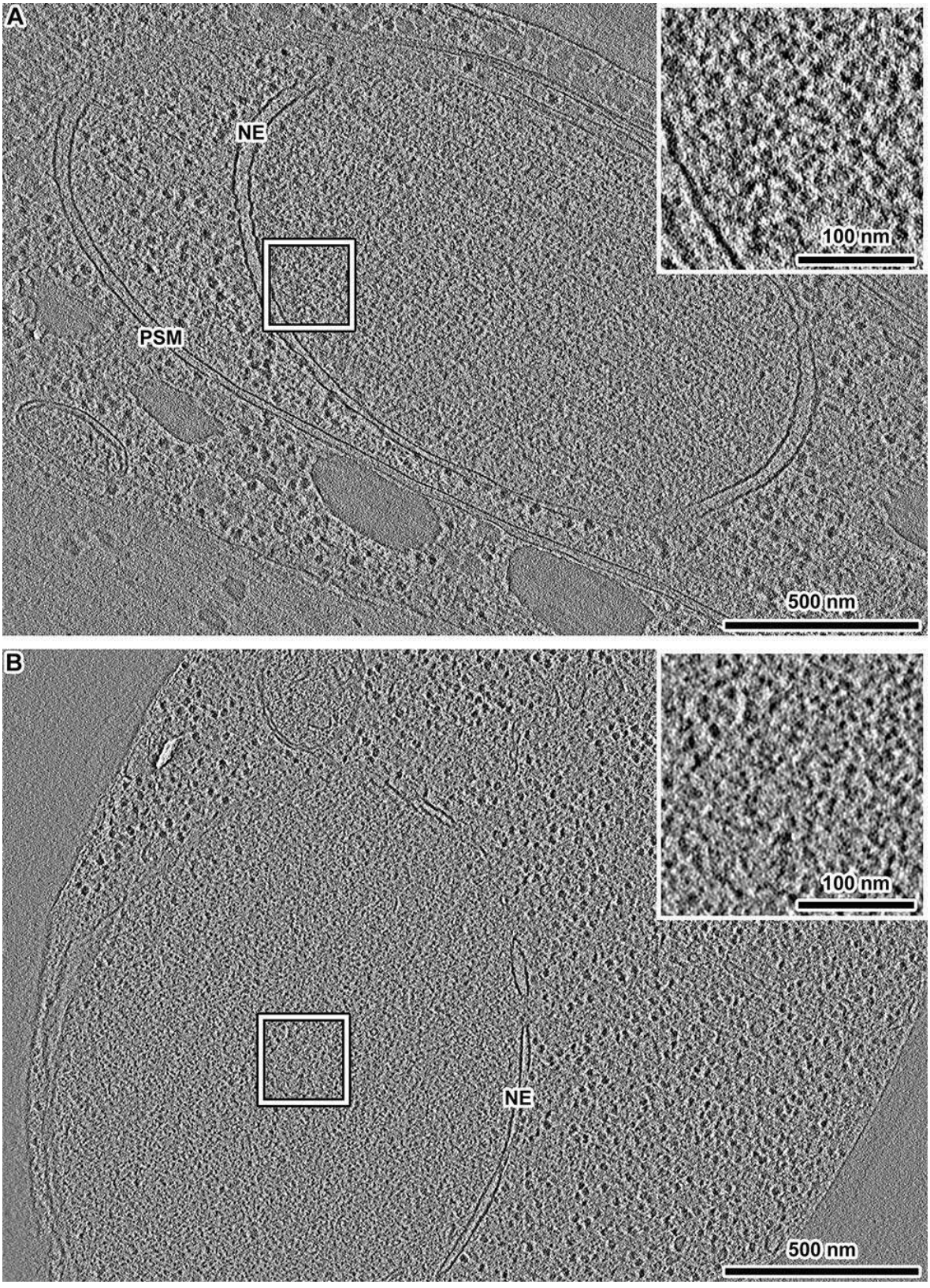

Figure S1. SC structures are not detected control cells

(A) Volta cryotomographic slice (12 nm) of a diploid yeast cell after an 8-hour incubation in SM. PSM, prospore membrane; NE, nuclear envelope. (B) Volta

cryotomographic slice (12 nm) of a haploid cell (strain W303) incubated 6 hours in SM. The insets show 3-fold enlargements of the nucleoplasm boxed in each panel.

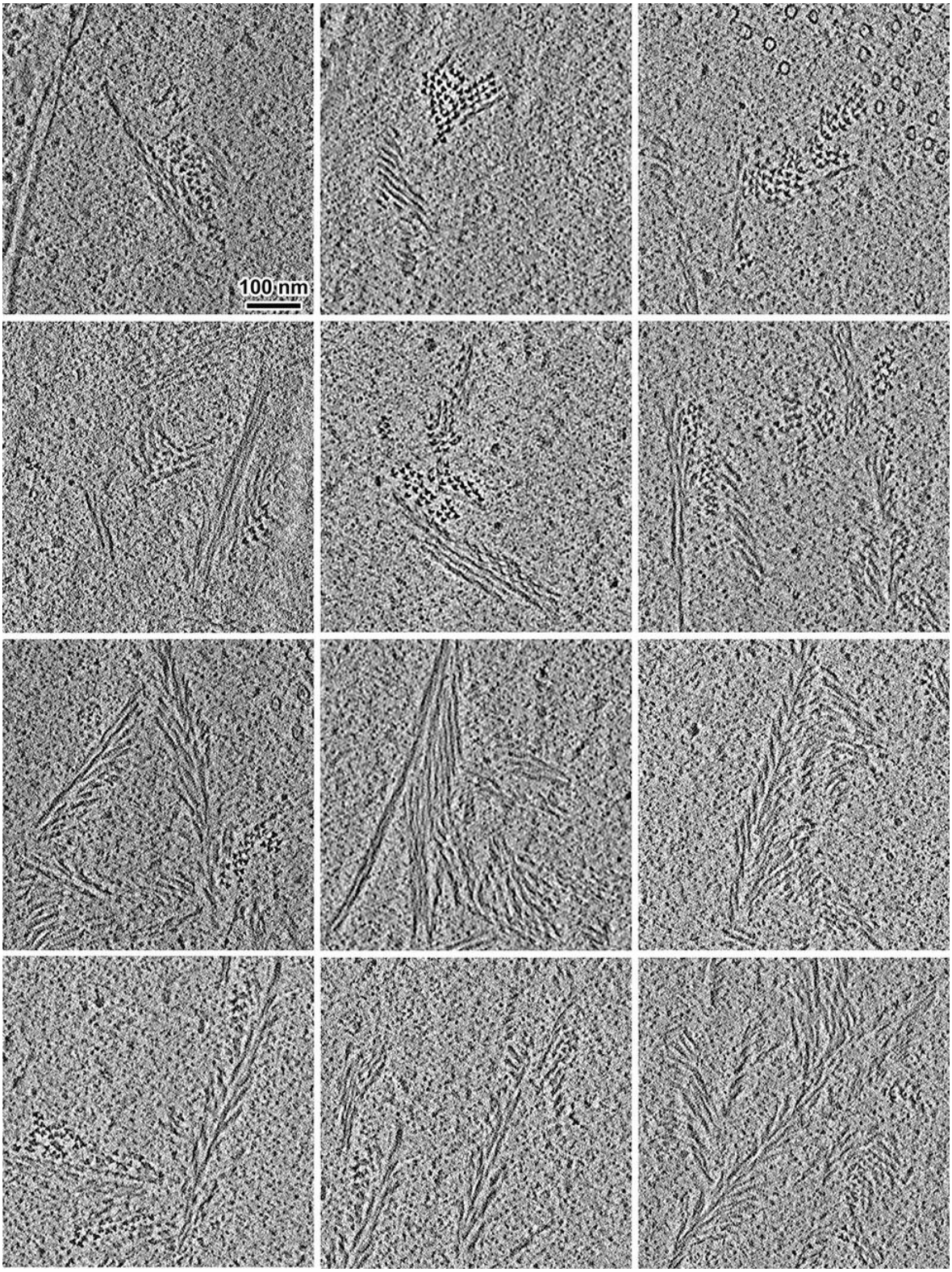

Figure S2. Examples of bundles of triple-helical filaments in pachytene cells
Volta cryotomographic slices (10 nm) of 12 examples of *ndt80*Δ *cell* nuclei after 8 hours in SM.

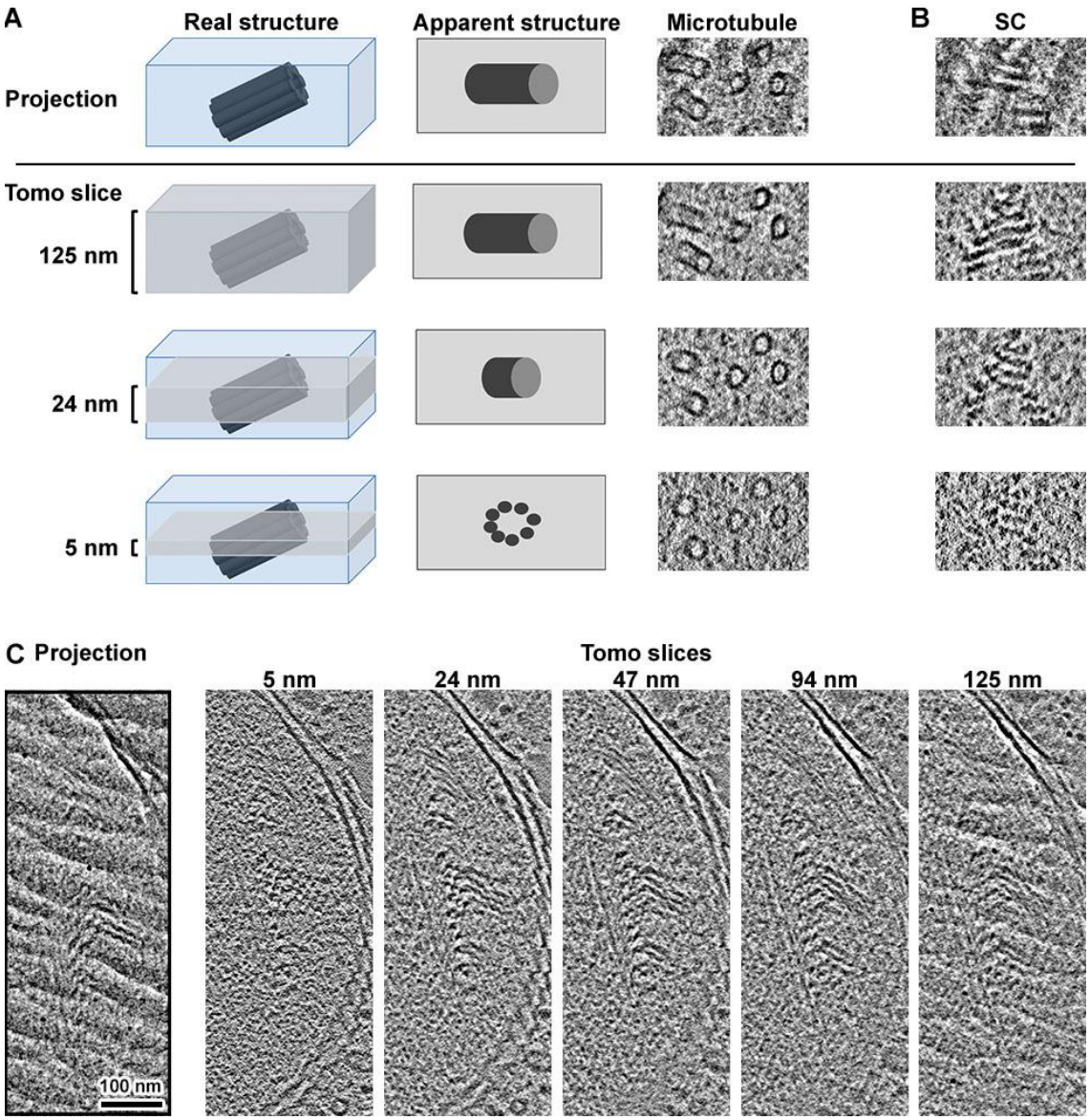

Figure S3. Comparison between tomographic slices and projections

(A) Cartoon of comparison between projection and tomographic slices of various thicknesses. Thin tomographic slices reveal details like microtubule protofilaments. Thicker tomographic slices resemble projection images. (B) In some projections, contiguous SC structures appear to orient approximately perpendicular (left-right) to the orientation of the filaments (out of the plane). (C) An SC position in a cell that has a chevron-like motif in projection. The thinner tomographic slices show that the underlying structure is a set of periodically packed triple-helical filaments that are slightly tilted from the axis out of the screen.

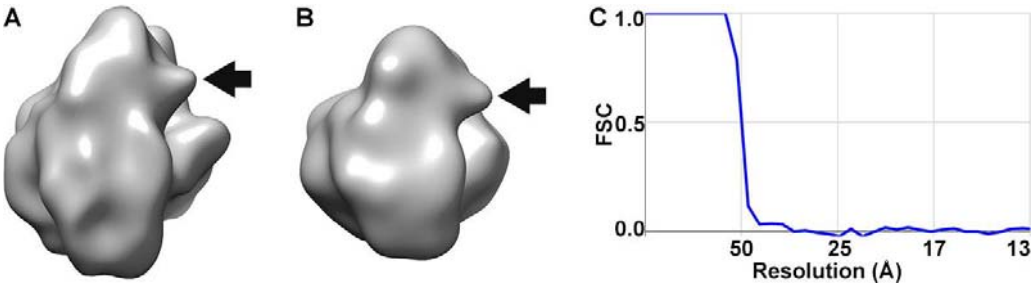

Figure S4. The cryotomograms have the correct hand

(A) Subtomogram average of cytoplasmic ribosomes from *ndt80*Δ cells. (B) Density map of the 80S yeast ribosome {Ben-Shem, 2011}, simulated at 35 Å resolution. The "beak" motif is indicated by an arrow in panels A and B. (C) FSC plot of the subtomogram average in panel A. The resolution is ~ 50 Å, based on the "Gold standard" FSC = 0.5 criterion.

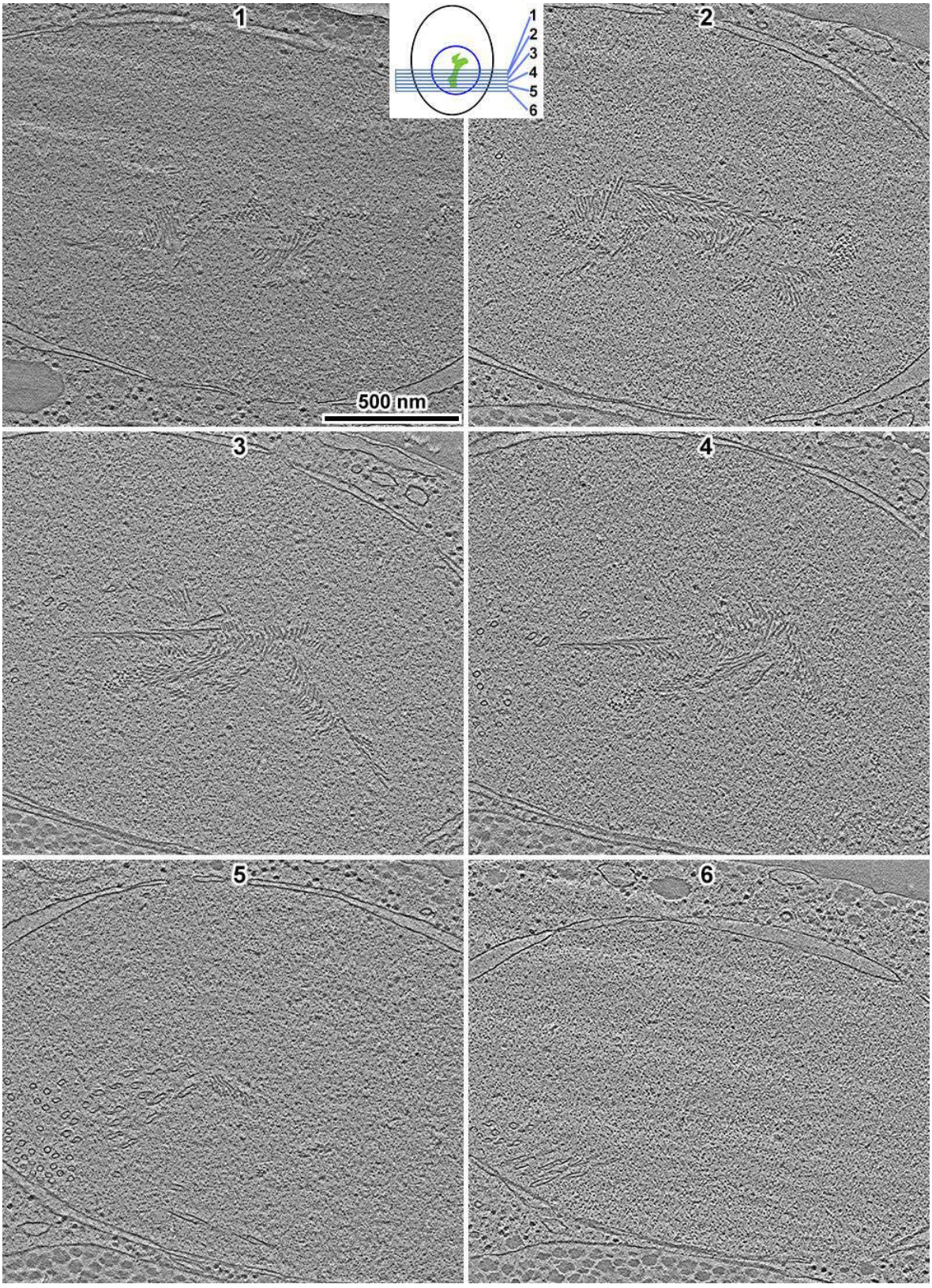

Figure S5. *ndt80*Δ SC triple-helical filaments are bundled throughout the cell

Volta cryotomographic slices of six sequential cryosections of a single *ndt80*Δ cell, isolated after 8 hours in SM. The schematic (not to scale) shows the relationship

between the numbered cryosections and the cytology. Major features are the cell nucleus (blue circle) and the SC filament bundles (green blob). The SC proteins in this cell are located in the center of the nucleus while the spindle is anchored at the lower left, with many microtubules visible in cryosections 4, 5, and 6.

Movie S1. *In situ* organization of the yeast SC

This movie summarizes our findings on the *in situ* 3-D packing of the SC filaments and their triple helical-structure. Please note that the movie includes both a narration and subtitles.

Table S1. Strains used

Strain	Key genotypic features	Experimental role	Origin
NKY611	SK1	WT	{Xu, 1995}, Surana lab
DK428 *	SK1, Zip1::GFP	WT, live fluorescence, 1,6-hexanediol perturbation	{Scherthan, 2007}
EW104	SK1, *ndt80*Δ, Zip1::GFP	Pachytene control, polycomplex induction	{White, 2004}
LY2	W303	Haploid control	Lacefield lab

* DK428 was formerly known as HW655

Table S2. Cryo-EM and image-analysis specifics.

EM grids	C-flat CF-4/2-2C (cryo) continuous carbon (plastic sections)
Cryomicrotome feed	70 or 100 nm
Microscope	TFS Titan Krios
Energy	300 keV
Camera: recording mode	TFS Falcon II: integration
Tomography software	TFS Tomo4
Calibrated pixel size	7.3, 5.8, or 4.6 Å
Contrast mechanism	Volta phase contrast
Defocus (nominal)	-0.5 or -1 µm
Cumulative dose	60 or 100 e^- / $Å^2$
Dose fractionation	1 / cosine
Tilt range	±60°, bidirectional, negative angles first
Tilt increment	2°
Tomogram processing	IMOD 4.10.22 beta
Template matching	PEET 1.13.0
Reference creation	Bsoft 1.8.8
Subtomogram analysis	RELION 3.0
Tomogram visualization	UCSF Chimera 1.13.1, IMOD 4.10.22 beta
Auxiliary scripts	https://github.com/anaphaze/ot-tools
Calculations	Google sheets, FIJI
Figure/movie editing	Adobe Photoshop, Illustrator, and Premiere Pro CC

Table S3. Cryotomogram details

Tomogram ID	Strain	SM time / treatment	Figure(s) / analysis	Dose	Pixel size (Å)	Defocus (µm)
20180629_139	NKY611	0h	2A	100	7.3	
20180816_32	DK428	2h	2B	100	5.8	
20180731_29	DK428	4h	2C	100	7.3	0.5
20181204_25	DK428	6h	2D	100	5.8	0.5
20180731_87	EW104	8h	3C	100	4.6	0.5
20181204_0hxd_01	DK428	6h	5B	100	5.8	0.5
20190322_17	DK428	6h/+5% hxd	5C, STA	70	4.6	0.5
20181204_7hxd_21	DK428	6h	5D	100	5.8	0.5
20190429_37	NKY611	4h	4A, B; 6B, D STA	100	5.8	0.5
20181204_25	DK428	6h	6A	100	5.8	0.5
20190429_76	NKY611	4h	6C, STA	100	5.8	0.5
20190109_35	DK428	8h	S1A	100	5.8	0.5
20190213_20	W303	6h	S1B	100	11.7	0.5
20180829_03	EW104	8h	S2	100	5.8	0.5
20180829_12	EW104	8h	S2	100	5.8	0.5
20180829_13	EW104	8h	S2	100	5.8	0.5
20180829_23	EW104	8h	S2	100	5.8	0.5
20180829_30	EW104	8h	S2	100	5.8	0.5
20180829_42	EW104	8h	S2	100	5.8	0.5
20180829_78	EW104	8h	S2	100	5.8	0.5
20180829_80	EW104	8h	S2	100	5.8	0.5
20180829_83	EW104	8h	S2	100	5.8	0.5
20180829_91	EW104	8h	S2	100	5.8	0.5
20180829_95	EW104	8h	S2	100	5.8	0.5
20180829_103	EW104	8h	S2	100	5.8	0.5
20181204_71	DK428	6h	S3C	100	5.8	0.5
20180829_24	EW104	8h	S5, #1	100	5.8	0.5
20180829_30	EW104	8h	S5, #2	100	5.8	0.5
20180829_58	EW104	8h	S5, #3	100	5.8	0.5
20180829_66	EW104	8h	S5, #4	100	5.8	0.5
20180829_74	EW104	8h	S5, #5	100	5.8	0.5
20180829_88	EW104	8h	S5, #6	100	5.8	0.5
20190429_03	NKY611	4h	STA	100	5.8	0.5
20190429_07	NKY611	4h	STA	100	5.8	0.5
20190429_19	NKY611	4h	STA	100	5.8	0.5
20190429_20	NKY611	4h	STA	100	5.8	0.5
20190429_29	NKY611	4h	STA	100	5.8	0.5
20190605_40	NKY611	4h	STA	100	4.6	0.5

20190605_41	NKY611	4h	STA	100	4.6	0.5
20190605_44	NKY611	4h	STA	100	4.6	0.5
20190605_77	NKY611	4h	STA	100	4.6	0.5
20190605_84	NKY611	4h	STA	100	4.6	0.5
20190605_85	NKY611	4h	STA	100	4.6	0.5
20190605_86	NKY611	4h	STA	100	4.6	0.5
20190605_90	NKY611	4h	STA	100	4.6	0.5
20190605_91	NKY611	4h	STA	100	4.6	0.5
20190322_01	DK428	6h / +5% hxd	STA	70	4.6	0.5
20190322_03	DK428	6h / +5% hxd	STA	70	4.6	0.5
20190322_04	DK428	6h / +5% hxd	STA	70	4.6	0.5
20190322_08	DK428	6h / +5% hxd	STA	70	4.6	0.5
20190322_35	DK428	6h / +5% hxd	STA	70	4.6	0.5
20190322_40	DK428	6h / +5% hxd	STA	70	4.6	0.5
20190322_41	DK428	6h / +5% hxd	STA	70	4.6	0.5
20180829_024	EW104	8h	STA	100	5.8	0.5
20180829_030	EW104	8h	STA	100	5.8	0.5
20180829_037	EW104	8h	STA	100	5.8	0.5
20180829_038	EW104	8h	STA	100	5.8	0.5
20180829_042	EW104	8h	STA	100	5.8	0.5
20180829_045	EW104	8h	STA	100	5.8	0.5
20180829_048	EW104	8h	STA	100	5.8	0.5
20180829_058	EW104	8h	STA	100	5.8	0.5
20180829_066	EW104	8h	STA	100	5.8	0.5
20180829_075	EW104	8h	STA	100	5.8	0.5
20180829_078	EW104	8h	STA	100	5.8	0.5
20180829_080	EW104	8h	STA	100	5.8	0.5
20180829_083	EW104	8h	STA	100	5.8	0.5
20180829_085	EW104	8h	STA	100	5.8	0.5
20180829_086	EW104	8h	STA	100	5.8	0.5
20180829_091	EW104	8h	STA	100	5.8	0.5
20180829_095	EW104	8h	STA	100	5.8	0.5

All data in this table were deposited as EMPIAR-#####. NKY611 = wild type; DK428 = wild type + Zip1-GFP; EW104 = *ndt80*Δ + Zip1-GFP. SM time = duration in sporulation medium. hxd = 1,6-hexanediol. STA = subtomogram averaging analysis. Dose, in electrons / $Å^2$; † Nominal (nom) and refined (ref) defocus values.

Table S4. Template-matching details

Complex	Reference	Grid spacing	Angular steps †	CC cutoff	low-pass filter	overlap limit
SC triple helix	30-nm tall, 12-nm diameter cylinder	16 nm	10°	0.2	60 Å	11 nm
Nucleosome	6-nm tall, 10-nm diameter cylinder	10 nm	10°	0.2	60 Å	6 nm
Ribosome	25-nm diameter sphere	30 nm	n/a	0.2	60 Å	30 nm

CC = cross-correlation. † Owing to the cylindrical symmetry of the reference used for the SC segments and nucleosomes, the angular search was not done around the cylindrical axis and was also limited to ± 90° around the other two axes. No angular search was done for ribosomes because the reference had spherical symmetry. If two template matching hits were positioned within the overlap limit, they were considered duplicates and one was removed automatically in PEET.